This manuscript has been submitted for publication in Geochimica et Cosmochimica Acta in October 2023. The manuscript has undergone one round of peer-review (with corrections submitted to journal) and has not yet been formally accepted for publication. Please note that subsequent versions may have slightly different content. Feel free to contact the authors with any questions or feedback.

Degree of sector zoning in clinopyroxene records dynamic magma recharge and ascent

Alice MacDonald[1*], Teresa Ubide[1], Silvio Mollo[2,3]

[1]School of the Environment, The University of Queensland, St Lucia, Queensland, 4072, Australia

[2]Department of Earth Sciences, Sapienza – University of Rome, P. le Aldo Moro 5, 00185 Roma, Italy

[3]Istituto Nazionale di Geofisica e Vulcanologia – INGV, Via di Vigna Murata 605, 00143 Roma, Italy

*Corresponding author: alice.macdonald@uq.edu.au

Abstract

The development of sector zoning in clinopyroxene is attributed to the influence of crystallisation kinetics imposed by magma undercooling (ΔT) and may reflect variations in magma cooling histories. Yet, the degree of compositional variations between sectors has not been explored as a potential recorder of crystallisation dynamics. Here, we investigate the distribution of major, minor, and trace elements between hourglass {- 1 1 1} and prism {*h k* 0} sectors in clinopyroxene with distinct pre-eruptive histories at Mt. Etna, Italy. We analyse sector-zoned clinopyroxene crystals ranging in size from sub-mm to cm (i.e., microphenocrysts, phenocrysts, and megacrysts), from eruptions fed by the central conduits of the volcano (1669 and 2002-03 flank eruptions) and eruptions fed by eccentric dykes which bypass the central conduits, tapping deeper magma storage regions (1974 and 2002-03 flank eruptions). We focus on Cr-rich mantle zones, which crystallised upon eruption triggering mafic recharge and are ubiquitous across our sample set. With decreasing crystal size (i.e., increasing ΔT), tetrahedral aluminium is more strongly partitioned between prism and hourglass sectors. This promotes the uptake of rare earth elements (REE) and high field strength elements (HFSE) into prism relative to hourglass sectors. Combining relative degrees of sector enrichment with ΔT estimates, we propose magma recharge, mush remobilisation and the onset of magma ascent imposed slightly higher ΔT in 1974 than in 2002-03 eruptions at Mt. Etna. Enhanced ΔT in 1974 could be related to vigorous mixing and rapid transport of magma with limited storage, resulting in crystals of smaller sizes. Crystal size populations vary across eruptions, but crystals within a given population (e.g., phenocrysts) return similar calculated ΔT and REE + HFSE sector enrichments, implying connectivity between magmatic environments in the mush system. We show that the magnitude of sector zoning in clinopyroxene can be employed to explore subtle differences in pre-eruptive dynamics in volcanic systems. As an example, we explore sector enrichment in

clinopyroxene phenocrysts from the 2021 eruption at La Palma (Canary Islands) and megacrysts from Roman era activity at Stromboli (Italy). Results highlight the role of dynamic mixing and mush remobilisation before eruption in steady-state mafic alkaline settings and suggest changes in magma composition across alkaline systems do not influence sector enrichment.

Keywords: Clinopyroxene, Sector zoning, LA-ICP-MS Mapping, Mt. Etna, Undercooling

1. Introduction

Textural and compositional variations in igneous minerals provide a critical means of understanding magmatic histories in volcanic plumbing systems. The sensitivity of mineral zoning to changes in the physical and chemical state of a magma can be utilised to decipher magmatic processes occurring in the lead up to volcanic eruptions (Putirka, 2008; Streck, 2008; Ubide and Kamber, 2018). Clinopyroxene is common in mafic to intermediate magmas and can be used to unravel magmatic histories in a range of volcanic settings (e.g., Neave et al., 2014; Mollo et al., 2015; Giacomoni et al., 2016; Di Stefano et al., 2020; Pontesilli et al., 2021; Ruth and Costa, 2021; Tapu et al., 2022). Due to its slow lattice diffusion compared to other volcanic minerals, such as olivine (Van Orman et al., 2001; Müller et al., 2013; Costa et al., 2020), sensitivity to changes in crystallisation conditions (Streck, 2008; Neave and Putirka, 2017; Mollo et al., 2018), and stability over a broad range of conditions (Armienti et al., 2007; Putirka, 2008; Mollo et al., 2015; Perinelli et al., 2016), clinopyroxene is able to store a protracted record of pre-eruptive processes as compositional zoning patterns. However, records of magmatic processes locked within clinopyroxene crystals are not always easily interpreted. In addition to concentric zoning associated with temporal changes in magma temperature, depth and composition, clinopyroxene crystals growing from a single melt may also be sector-zoned, with distinct chemical compositions growing along different crystallographic orientations. Sector-zoned crystals consist of ‘hourglass’ sectors {- 1 1 1},

growing rapidly along the *c*-axis, and coeval 'prism' sectors {*h k* 0}, growing relatively slowly perpendicular to the *c*-axis, with a distinct composition (Leung, 1974; Dowty, 1976; Ubide et al., 2019a). Typically, hourglass sectors are enriched in Si compared to prism sectors, which incorporate higher amounts of Al substituting for Si in the tetrahedral site, and highly charged cations such as Ti balancing the charge deficit in the M1 site (Ubide et al., 2019a; Di Fiore et al., 2021).

$$[^{T}Si^{4+},^{M1}Mg^{2+}]_{\{-1\,1\,1\}} \leftrightarrow [^{T}Al^{3+},^{M1}Ti^{4+}]_{\{h\,k\,0\}} \quad (1)$$

Charge imbalance due to Si ↔ Al substitution causes an increased uptake of highly charged trace cations, such as rare earth elements (REE) and high field strength elements (HFSE) into prism sectors. Therefore, Eq. (1) can be re-evaluated in terms of clinopyroxene and trace element partitioning between sectors as (Ubide et al., 2019a; MacDonald et al., 2022):

$$[Di]_{\{-1\,1\,1\}} \leftrightarrow [REETs + HFSETs]_{\{h\,k\,0\}} \quad (2)$$

Where *REETs* and *HFSETs* (*Ts* = $CaAl_2SiO_6$ + $CaFeSiAlO_6$) are hypothetical clinopyroxene Tschermak components, which along with diopside *Di* ($CaMgSi_2O_6$) express the major cation distributions in the lattice site of clinopyroxene. The occurrence of sector zoning can be attributed to a combination of the architecture of crystal faces, the relative diffusion of cation species in the melt, and the relative growth rates of clinopyroxene along different crystallographic axes (Nakamura, 1973; Downes, 1974; Leung, 1974; Dowty, 1976; Shimizu, 1981; Mollo et al., 2023), driven by magma undercooling ($\Delta T = T_{liquidus} - T_{crystallisation}$; Kirkpatrick 1981). Experimentally, the presence of sector zoning in clinopyroxene in mafic alkaline systems has been observed at low ΔT, associated with interface growth kinetics at near-equilibrium conditions (ΔT < 45 °C; Kouchi et al., 1981; Masotta et al., 2020). Undercooling exerts a significant influence on crystal morphology, size and chemistry (Dowty, 1980; Kouchi et al., 1983; Shea and Hammer, 2013; Mollo and Hammer, 2017;

MacDonald et al., 2022), and can be induced in a magma by cooling, mixing, or exsolution of H_2O, which may be driven by decompression (e.g., Ubide et al., 2021). The presence and degree of sector zoning can also indicate magma ΔT (Kouchi et al., 1983; Ubide et al., 2019a; Mollo et al., 2023), and larger compositional contrasts between sectors have been observed in plagioclase crystals at increasing cooling rates (Lofgren, 1980; Smith and Lofgren, 1983). However, the relationship between ΔT and the extent of elemental partitioning between sectors remains underexplored. In clinopyroxene, a better understanding of the impact of magma ΔT on zoning may provide new insights into processes of cooling and degassing associated with distinct magmatic pathways and ascent in mafic to intermediate settings (Mollo et al., 2013, 2023; Ubide et al., 2019a; Masotta et al., 2020; MacDonald et al., 2022). Here, we investigate the compositional contrasts between sectors in clinopyroxene microphenocrysts, phenocrysts and megacrysts from eruptions fed by distinct pathways at Mt. Etna, Italy, to investigate the effects of both crystal size and magmatic pathway on the development of sector zoning. Mt. Etna is one of the most active, and well monitored, volcanoes in Europe. Eruptions can be classified as either 'central conduit', where magma travels through the complex central conduit system, or less commonly 'eccentric', where magma bypasses the central conduit and travels rapidly to the surface, undergoing minimal degassing (Clocchiatti et al., 2004; Métrich et al., 2004; Corsaro et al., 2009; Fig. 1). Clinopyroxene is common in products of both eruption types and is stable across most of the vertically extensive plumbing system, as outlined by thermodynamic modelling and thermobarometry (Armienti et al., 2007; Armienti et al., 2013). Concentric zones enriched in Cr and Mg and depleted in REE and HFSE are common close to crystal rims and testify to mafic recharge as a typical eruption trigger from a main storage region located at a depth of ~10 km (Ubide and Kamber, 2018). Here, we focus on these zones, which we refer to as Cr-rich mantles to differentiate them from the outermost, Cr-poor rims which are interpreted as

recorders of final crystallisation upon ascent and eruption (Ubide and Kamber, 2018). We apply high resolution laser ablation mass spectrometry mapping techniques to explore the degree of partitioning between sectors in Cr-rich mantles across crystal sizes and eruption types and assess the relationship with between sector partitioning and inferred ΔT. Our results provide insights into the roles of magmatic pathways and crystal sizes on the development of sector zoning in clinopyroxene from a range of alkaline magma compositions.

2. Materials and Methods

2.1. Samples

This study uses a variety of sector-zoned clinopyroxene crystals from the 1669, 1974 and 2002-03 eruptions at Mt. Etna (see Fig. S1 for photomicrographs). We use the largest crystal size population from each eruption as best representative of magma storage; 1) megacrysts from the 1669 eruption, 2) phenocrysts from the 2002-03 central conduit and eccentric eruptions, and 3) microphenocrysts from the 1974 eruption. Groundmass compositions from all eruptions studied here are trachybasalts (Fig. S2), with similar concentrations of SiO_2 (~ 48 wt. %) and Al_2O_3 concentrations varying from 16.4 wt. % (1974 eccentric) to 19.1 wt. % (1669). The 1669 eruption was fed by the central conduit, generating a monogenetic cone on the southern flank of the volcano (Monti Rossi) and an extensive lava field that reached part of the city of Catania (Corsaro et al., 1996; Mulas et al., 2016; Kahl et al., 2017; Magee et al., 2020), erupting lavas with plagioclase, clinopyroxene, and olivine phenocrysts (Corsaro et al., 1996; Kahl et al., 2017; Fig. S2a). We use clinopyroxene megacrysts (> 5000 µm length) from weathered scoria fragments collected from the crater rim of the Monti Rossi scoria cone and previously described by Magee et al. (2020). This former study focused on core to rim oscillatory zoning using megacrysts mounted perpendicular to the *c*-axis to minimise the effect of sector-zoning. Here, we use clinopyroxene megacrysts from the same sample set,

mounted parallel to the *c*-axis to effectively investigate sector zoning (Fig. S1a).

We also use clinopyroxene phenocrysts (1000 – 5000 μm length, Fig. S1 c-d) from samples erupted during the 2002-03 fissure eruption, with simultaneous outpourings of trachybasaltic lava at the north-east rift (central conduit) and south rift (eccentric) of the volcano (Clocchiatti et al., 2004; Andronico et al., 2005). We select samples previously characterised in Magee et al. (2021), who focused on elemental and isotope variations in matrix geochemistry on timescales of days to months. Although groundmass compositions from both eccentric and central conduit eruptions classify as trachybasalts (Fig. S2a), their mineralogy differs. Lavas from the central conduit eruptions have abundant phenocrysts, including plagioclase, clinopyroxene and olivine with titanomagnetite inclusions. In contrast, plagioclase is absent as a phenocryst phase in eccentric lavas (Kahl et al., 2015; Magee et al., 2021). Here, we adopt the term 'phenocryst' strictly to refer to crystal size, not the origin of these crystals.

We integrate results from the 1669 megacrysts and 2002-03 phenocrysts with microphenocrysts erupted in the 1974 eccentric eruption reported in Ubide et al. (2019a). The 1974 eccentric eruption generated two scoria cones and associated trachybasaltic lava flows on the western flank of the volcano, concomitant with minor summit activity (Corsaro et al., 2009). Lavas contain clinopyroxene and olivine microphenocrysts, with plagioclase only present as a groundmass phase. We test if decreasing crystal sizes from megacrysts to microphenocrysts in the studied sample suite, inferred to reflect increasing nucleation rates and magma undercooling, impacts the degree of compositional enrichment of prism sectors relative to hourglass sectors in clinopyroxene.

2.2 Analytical methods

Major element compositions of clinopyroxene megacrysts from the 1669 eruption were determined by electron probe microanalysis (EPMA) on carbon coated resin mounts using a JEOL JXA 8530F Hyperprobe equipped with five wavelength dispersive spectrometers at the Central Analytical Research Facility (CARF) at the Queensland University of Technology, Australia. Analyses used an accelerating voltage of 15 kV, a beam current of 30 nA and a beam size of 3 μm. Line transects were conducted across hourglass and prism sectors, and across concentric zones within sectors, with variable spacings between points. In addition, manually selected points targeting hourglass and prism sectors were also used, resulting in a total of 75 analytical points for mantles. Counting times for elements were 20 s on and off peak for all elements; except Cr and Ni, which were counted for 30 s on and off peak, and Na which was counted for 10s on peak and 10s off peak. The instrument was calibrated using: NBS K411 glass (Si-TAP, Mg-TAPH), rutile (Ti-LIFH), plagioclase (Al-TAP), Cr oxide (Cr-LiFL), hematite (Fe – LIFH), Rhodonite (Mn – LIFH), Ni90Fe10 alloy metal (Ni – LiFL), wollastonite (Ca – PETJ) and albite (Na – TAPH) standards. To monitor data quality, we routinely analysed an in-house clinopyroxene standard (Table S1). Accuracy was typically better than 4%, except for Ni which was typically below the detection limit. Precision was typically better than 2% for major elements > 1 wt.% abundance, and better than 5% for minor elements < 1 wt.% abundance. Precision based on EPMA-outputted uncertainties yield similar results, with precision typically better than 1% for elements > 1 wt. % abundance, and better than 6% for elements < 1 wt.% (Table S3). Results were filtered using mineral stoichiometry and analytical totals. Major element compositions for the 2002-03 eccentric phenocrysts and 1974 microphenocrysts are from Ubide et al. (2019a).

We used laser ablation inductively coupled mass spectrometry (LA-ICP-MS) to produce trace element maps of clinopyroxene crystals from the 1669 and 2002-03 eruptions, following the method of Ubide et al., (2015). Mapping areas for the 1669 megacrysts were selected using

EPMA imaging and analyses, including both hourglass and prism sectors. Sector-zoned crystals from the 2002-03 eruptions were selected using thin section microscopy. Analyses were conducted at The University of Queensland Centre for Geoanalytical Mass Spectrometry, Radiogenic Isotope Facility (UQ RIF-lab), using an ASI RESOlution 193 nm excimer UV ArF laser ablation system with a dual-volume Laurin Technic ablation cell and GeoStar Norris software, in conjunction with a Thermo iCap RQ quadrupole mass spectrometer and Qtegra software. Ablation was conducted under ultrapure He conditions, with trace N_2 and Ar make up gas to aid in efficient transport and ionisation of ablated material. The instrument was calibrated using NIST612 glass reference material prior to analysis. A range of square spot sizes were used, depending on the crystal size and target area. For the 1669 megacrysts, we used 30 × 30 µm, with a scan speed of 30 µm/s, a repetition rate of 10 Hz and a fluence of 3 J/cm^2, with a path separation of 1 µm. For the 2002-03 eccentric and central conduit phenocrysts, we used smaller square spot sizes of 12 × 12 µm or 20 × 20 µm, corresponding to scan speeds of 12 µm/s or 20 µm/s, respectively. Each crystal was analysed twice with different sets of analytes, following Ubide et al. (2019a). The first analyte menu included ^{7}Li, ^{23}Na, ^{27}Al, ^{43}Ca, ^{45}Sc, ^{49}Ti, ^{51}V, ^{52}Cr, ^{60}Ni, ^{88}Sr, ^{90}Zr, ^{93}Nb, ^{178}Hf and ^{181}Ta, with a total sweep time of 147 ms. The second analyte menu included ^{43}Ca, ^{89}Y, ^{139}La, ^{140}Ce, ^{141}Pr, ^{146}Nd, ^{147}Sm, ^{153}Eu, ^{157}Gd, ^{159}Tb, ^{163}Dy, ^{165}Ho, ^{166}Er, ^{169}Tm, ^{172}Yb and ^{175}Lu, with a sweep time of 195 ms. Additional trace element maps of 2002-03 clinopyroxene phenocrysts were produced using a QuadLock (©Norris Scientific) add-on for the LA ICP-MS system, and a Fast Funnel (©Norris Scientific) adaptor add-on for the laser ablation cell. The ablation cell was connected to the ICP-MS using a small diameter tube (1 mm inner diameter), with a short length (~60 cm) which allowed for faster washout times. For maps produced using this technique, we used a square spot size of 12 × 12 µm, a scan speed of 40 µm/s, a repetition rate of 74 Hz and a fluence of 3 J/cm^2. We also produced

maps using a square spot size of 20 × 20 µm and a scan speed of 60 µm/s for larger crystals. We used a single analyte menu, combining the menus outlined previously, with a total dwell time of 165 ms.

Trace element maps were produced using Iolite v4 (Paton et al., 2011) in quantitative mode. We used NIST612 glass reference material as the calibration standard for all analytes, except Ti and Cr for which we used BHVO-2G glass reference material. Calcium concentrations measured by EPMA are typically homogenous in our crystals and therefore used as the internal standard: 21.7 wt. % CaO for 1669 megacrysts and 22.2 wt. % CaO for 2002-03 crystals. BCR-2G, GSD-1G and BHVO-2G glass reference materials were routinely measured during analytical sessions to monitor data quality (Table S2). For the first mapping technique described (regular mapping), accuracy was better than 10 % and precision was better than 5 %**.** For the fast-mapping technique, accuracy was better than 15 % and precision was better than 7 %. Trace element concentrations were extracted using the Monocle add-on for Iolite, using the 'from selections' option (Petrus et al., 2017). We extracted data from individual hourglass and prism sectors from Cr-rich mantles recording magma recharge (e.g., Ubide and Kamber, 2018). We used Cr and Zr compositional maps to locate and extract data from hourglass and prism sectors within mantle zones. We also used Ca maps to ensure that cracks and inclusions were avoided. Trace element data for the 1974 microphenocryst are from Ubide et al. (2019a).

3. Results

3.1. Clinopyroxene Cr-rich mantles

The clinopyroxene crystals analysed in this study are typically euhedral, ranging in sizes from megacrysts (8 – 12 mm length), to phenocrysts (1 – 4 mm) and microphenocrysts (350 – 800 µm; Fig. S1), and classify as diopside-augites following the classification scheme of

Morimoto (1988; Fig. S2b). All crystals are sector-zoned, with Cr-rich mantles and Cr-poor outermost rims which transect the sectors (see Fig. 2, Fig. **S3**). Many crystals also contain cores (Fig. 2), which are resorbed to variable degrees, and may also be sector-zoned. We focus on Cr-rich mantles to explore the development of sector zoning associated with magma recharge across crystal sizes and eruption types, noting that in the 2002-03 eruption, clinopyroxene with Cr-rich mantles is more common in eccentric samples than in in central conduit samples (Magee et al., 2021; Fig. S4). Although the Cr-poor outermost rims may also be sector-zoned, many crystals from the 1974 and 2002-03 eccentric activity only have very thin rims (< 35 µm in prism sectors), hindering analysis and a comprehensive comparison across eruption types and crystal sizes.

We compare major and minor element compositions collected from 1669 hourglass and prism sectors in Cr-rich mantle zones to previously published major element data for sector-zoned crystal mantles from the 1974 and 2002-03 eccentric eruptions (Fig. 3; Ubide et al., 2019a), and a compilation of clinopyroxene compositions from Mt. Etna from GEOROC (https://georoc.eu; Table S5). Data collected for the 1669 megacrysts is provided in Table S3, and previously published data in Table S4. Broadly, hourglass sectors have higher Mg#, expressed as MgO / (MgO + FeO_t) × 100 on molar basis, and lower ^{T}Al and ^{M1}Ti contents than corresponding prism sectors. This compositional variation leads to an increase of *Ts* in prism sectors at the expense of *Di*, following Eq (2). On the other hand, ^{M2}Ca and ^{M2}Na remain constant across sectors for all crystal sizes and eruptions, consistent with previous studies regarding the incorporation of major elements across clinopyroxene sectors at Mt. Etna (Downes 1974, Duncan and Preston 1980, Ubide et al., 2019a; Mollo et al., 2023), and for augitic clinopyroxenes in other systems (Hollister and Gancarz 1971, Leung 1974).

In general, clinopyroxene compositions studied here are similar to those previously published at Mt. Etna (Fig. 3). Clinopyroxene mantles from the 1669 eruption have higher ^{M2}Na and

lower ^{T}Al and ^{M1}Ti contents than clinopyroxene mantles with the same Mg# from the 1974 and 2002-03 eccentric eruptions. Interestingly, the average ^{T}Al content shows that prism sectors in the 1669 megacrysts is lower (0.19 ± 0.01 apfu) than in prism sectors in 1974 microphenocrysts (0.28 ± 0.04 apfu) and 2002-03 phenocrysts (0.22 ± 0.02 apfu). In contrast, hourglass sectors in the 1669 megacrysts have ^{T}Al contents (0.15 ± 0.02 apfu) comparable with those from 1974 (0.14 ± 0.02 apfu) and 2002-03 (0.13 ± 0.02 apfu). This effect is illustrated with kernel density estimates in Fig. 4, and suggests that the decrease in crystal size, inferred to reflect increasing nucleation rate at the expense of growth rate upon larger ΔT, results in an increasing departure of prism compositions from hourglass sectors.

3.2. Trace element compositional mapping

LA-ICP-MS trace element maps of clinopyroxene megacrysts, phenocrysts and microphenocrysts highlight the distinct distribution of trace elements between sectors across the range of eruptions and crystals sizes studied (Fig. 2; compositional data in Table S6 and additional maps in Fig. S4). The concentration of HFSE (e.g., Zr and Ta) and REE (e.g., Ce and Yb) follows Al zoning, with higher concentrations in prism sectors compared to hourglass sectors, according to charge balance substitutions previously highlighted in natural and experimental studies (Ubide et al., 2019a; Di Fiore et al., 2021; MacDonald et al., 2022). Importantly, we observe that sector partitioning dominates across a range of eruption styles and crystal sizes at Mt. Etna.

Trace element maps also reveal that Cr zoning is mainly concentric and associated with mafic recharge, with comparatively minor partitioning between sectors (Fig. 2). Concentric zones in these crystals crosscut hourglass and prism sectors, highlighting coeval growth of Cr-rich mantle zones across clinopyroxene sectors. The arrival of hot, mafic magma into the system causes resorption of cores and growth of Cr-rich mantle zones (Streck, 2008; Ubide and Kamber, 2018). Across the range of crystals analysed in this study, the degree of Cr

enrichment in mantle zones can vary from 240 to 1265 ppm in prism sectors, attesting to variable degrees of mafic recharge across eruptions (e.g., Ubide and Kamber 2018) and spatial variability of mafic invasion and mixing in the reservoir (Cashman and Blundy, 2013; Bergantz et al., 2015; Magee et al., 2020). In addition, many crystals from the 2002-03 central conduit eruption may not record magma recharge and hence not contain mantle zones following the definition used here (e.g., Fig. S4), supporting the notion of mafic intrusions being diluted through the central conduits and more effectively tapped through eccentric dykes at Mt. Etna (Clocchiatti et al., 2004; Ubide and Kamber, 2018; Magee et al., 2021) and other mafic volcanoes (e.g., Ubide et al., 2023).

4. Discussion

4.1. Sector zoning across variable magmatic pathways and crystal sizes

Our set of crystals encompass a range in crystal sizes and eruption types at Mt. Etna, providing a natural dataset to test the relationship between magma undercooling and the extent of sector zoning in clinopyroxene. Different eruptive pathways may be associated with variable magmatic conditions, including temperature, pressure, crystal residence time and ascent, degassing, and cooling rate (Armienti et al., 2013; Kahl et al., 2015). Magma dynamics modulate ΔT and hence, the composition, texture, and development of sector zoning of clinopyroxene (Mollo et al., 2013, 2023; Ubide et al., 2019a; Masotta et al., 2020). In addition to magma ascent pathways, the range of crystal sizes across our suite of samples also attest to differences in clinopyroxene growth rates, which are also associated with different ΔT (Kouchi et al., 1983; Mollo and Hammer, 2017; Masotta et al., 2020; Moschini et al., 2021).

As observed in trace element maps (Fig. 2), relative enrichments in HFSE + REE in prism relative to hourglass sectors are directly controlled by Equations (1) and (2), which is energetically more favourable than mechanisms relevant to aegirine-rich clinopyroxenes in

297 highly alkaline systems (Beard et al., 2019; Bernard et al., 2020). The observed sector
298 partitioning is typical of sector zoning at Mt. Etna and other mafic alkaline settings
299 (Nakamura, 1973; Ubide et al., 2019a, 2019b) and has been shown experimentally to be
300 influenced by ΔT (Grove and Bence, 1979; Kouchi et al., 1983; Mollo et al., 2013, 2018,
301 2023; Masotta et al., 2020; MacDonald et al., 2022). Due to the influence of $^{T}Si \leftrightarrow {}^{T}Al$
302 substitution on the uptake of trace cations, we first investigate the distribution of ^{T}Al between
303 sectors and then explore the degree of enrichment of trace cations in prism relative to
304 hourglass sectors, which we hereafter refer to as 'sector enrichment.'
305 The difference in ^{T}Al between hourglass and prism sectors differs significantly between
306 samples (Fig. 4). Megacrysts from the 1669 eruption have the lowest difference in ^{T}Al across
307 sectors ($\Delta^{T}Al$ = 0.04 apfu), followed by phenocrysts from the 2002-03 eccentric eruption
308 ($\Delta^{T}Al$ = 0.09 apfu) and microphenocrysts from the 1974 eccentric eruption ($\Delta^{T}Al$ = 0.14
309 apfu). Hourglass sectors define similar hourglass ^{T}Al peak (Fig. 4) but prism sectors define
310 distinct ^{T}Al peaks across clinopyroxene sizes (Fig. 4). Prism ^{T}Al contents and the difference
311 between prism and hourglass compositions, increase with decreasing crystal size, consistent
312 with increasing nucleation rates, and decreasing growth rates with increasing ΔT (e.g., Mollo
313 and Hammer, 2017). It follows that ^{T}Al sector enrichment reflects key differences in
314 crystallisation conditions associated with mafic recharge events across eruptions.
315 To further explore the degree of sector zoning across samples and quantify its relationship
316 with ΔT, we focus on trace element partitioning between sectors (Fig. 5). Previous works
317 based on natural (Ubide et al., 2019a) and experimental (MacDonald et al., 2022)
318 observations of sector-zoned clinopyroxene from Mt. Etna suggested that the degree of sector
319 enrichment of trace elements in prism relative to hourglass sectors may be a proxy for magma
320 ΔT. To quantify the degree of sector enrichment of a cation, we divide the concentration of
321 that cation in the prism sector by that of the hourglass sector {*h k 0*}/{- 1 1 1}, previously

322 defined as enrichment factor in Shimizu (1981) and then applied to clinopyroxene
323 microphenocrysts from Mt. Etna (Ubide et al., 2019a) and other tectonic settings (Wang et
324 al., 2022). We compare the degree of sector enrichment to the ionic potential of a cation
325 (Z/r^2), where Z is the charge of the cation and r is the ionic radius from Shannon (1976) (Fig.
326 5; Table S7). For a given crystallographic site, the increase in ionic potential correlates with
327 enhanced development of sector zoning, as quantified by the increase in sector enrichment
328 (Fig. 5a).
329 Cations with low ionic potential in M1 and M2 sites (i.e., low charge cations Li, Na, Ni and
330 Sr) are typically not sector-zoned due to their inefficiency as charge balancing cations (Fig. 5;
331 Ubide et al., 2019a). In addition, the degree of sector enrichment of these low-charge cations
332 does not systematically vary between different crystal sizes and eruptions, despite differences
333 in ^{T}Al content and sector zoning (Fig. 4).
334 Following the IUPAC definition for Sc as a transition metal (i.e., an element forming ions
335 with partially filled *d* orbitals in common settings), we note that Sc and Cr are weakly
336 partitioned between hourglass and prism sectors. Crystal field effects may be more influential
337 in the incorporation of Cr in clinopyroxene compared to local charge balance mechanisms
338 associated with ^{T}Si ↔ ^{T}Al substitutions (Di Fiore et al., 2021; Mollo et al., 2023), resulting in
339 the relative insensitivity of Cr to sector zoning.
340 As the ionic potential increases from tetravalent HFSE (Zr, Hf) to pentavalent HFSE (Ta, Nb)
341 cations in the M1 site, the degree of sector enrichment increases from megacrysts to
342 microphenocrysts (Fig. 5a). The relationship between crystal size and sector enrichment
343 broadly holds for HFSE as a function of ^{T}Al incorporation in prism and hourglass sectors
344 (Fig. 4). Ta is more variable than tetravalent HFSE across our samples due to its higher
345 charge (see MacDonald et al., 2022), with average enrichment factors ranging between 4.5 ±
346 0.8 (1974 microphenocrysts) and 1.9 ± 0.01 (1669 megacrysts). In comparison, Zr has

enrichments factors which vary from 2.1 ± 0.2 (1974 microphenocrysts) to 1.4 ± 0.02 (1669 megacrysts). The contrast between tetravalent and pentavalent HFSE highlights the effect of ionic charge on sectoral partitioning, as previously suggested by Ubide et al., (2019a).

The isovalent REE series is expanded in Fig. 5b to explore differences in sector enrichment across crystal populations and eruption types. The 1974 microphenocrysts exhibit the highest degree of sector enrichment of our sample set, in accordance with the highest ^{T}Al contrast between sectors (Fig. 4). This attests to the importance of charge-balancing substitution mechanisms in the uptake of REE into the M2 site, as the probability of REE entering a charge-neutral site increases with increasing ^{T}Al (Blundy et al., 1998; Hill et al., 2000; Wood and Blundy, 2001; Mollo et al., 2013, 2018, 2020). With the increase in size from 2002-03 phenocrysts to 1669 megacrysts, sector enrichment decreases across the REE (Fig. 5b), supporting the link between undercooling, growth rate and trace element incorporation.

We note that sector enrichment decreases with ionic potential from light to heavy REE, with higher variability of LREE (e.g., La, Ce) across crystal sizes and samples compared to HREE (e.g., Lu, Y in Fig. 6). This suggests that HREE may be less influenced by the entry of ^{T}Al, compared to LREE, as previously observed in experimental studies (MacDonald et al., 2022). Average sector enrichments for La and Lu (as proxies for LREE and HREE respectively) shows that sector enrichments are stronger in the 1974 microphenocrysts (La = 1.8 ± 0.1, Lu = 1.5 ± 0.2) than in 2002-03 phenocrysts (La = 1.6 ± 0.05 , Lu = 1.4 ± 0.1) and 1669 megacrysts (La = 1.3 ± 0.04, Lu = 1.2 ± 0.04), which potentially crystallised under decreasing ΔT.

In summary, as the difference in ^{T}Al between sectors increases, HFSE and REE are more enriched in prism sectors relative to simultaneously growing hourglass sectors, resulting in higher degrees of sector enrichment. To explore the relationship between sector enrichment and crystallisation dynamics associated with pre-eruptive magma recharge, influencing

crystal size and the development of sector zoning in our crystals, we plot the sector enrichments of a range of HFSE and REE against crystal width in Fig. 6.Crystallographic contrasts in sector-zoned clinopyroxene in mafic alkaline systems reflect the interplay of relative growth rates between sectors, diffusion of cations in the melt and geometric distribution of lattice sites between crystal faces as induced by ΔT, causing the development of compositionally distinct local melts which feed crystal growth (Hollister and Gancarz, 1971; Nakamura, 1973; Downes, 1974; Leung, 1974; Dowty, 1976; Mollo et al., 2023). Specifically, the preferential uptake of Si and Mg in hourglass {- 1 1 1} sectors in augitic clinopyroxene can be attributed to the simultaneous exposure of M and T sites, requiring both divalent cations and silica tetrahedra (Nakamura 1973; Leung, 1974), ultimately resulting in the depletion of Si and Mg and enriched in cations such as Al, Ti and Fe in the melt adjacent to hourglass sectors (Leung, 1974). On the other hand, prism {h k 0} sectors have alternating exposed layers of M and T sites, therefore requiring large amounts of these cations to facilitate growth, enabling the accommodation of cations such as Al and Ti and ultimately causing their depletion in the melt adjacent to prism sectors (Nakamura, 1973; Leung, 1974). Importantly, when T site layers are exposed, rapid depletion of Si in the local melt results in its substitution with Al, and this effect is enhanced in undersaturated liquids (Leung, 1974). Following this principle, the degree of sector enrichment of Al and subsequently, HFSE and REE, is expected to increase with ΔT (Mollo et al., 2023). Under kinetic growth conditions, crystal growth is driven by ΔT, which approximates melt supersaturation phenomena arising from concentration-dependent reactions induced by interface kinetics (Mollo and Hammer, 2017). Therefore, initial concentration gradients in the melt at the crystal-melt interface are counterbalanced by diffusive relaxation that becomes more effective over crystallisation timescales (i.e., the crystal residence time). Following this logic, the growth rate of clinopyroxene decreases as the crystal residence time increases and approaches zero as the

melt relaxes towards an equilibrium state where concentration gradients cease (Pontesilli et al., 2019; Moschini et al., 2021). Decreasing ΔT promotes a decrease in maximum crystal growth rate, leading to a steady-state textural maturation of polyhedral crystal forms (Mollo and Hammer, 2017). The combination of long residence times and low ΔT mitigates the compositional contrast between melts feeding the growth of different crystal faces, thereby lowering the degree of sectoral enrichment in clinopyroxene. The growth of clinopyroxene megacrysts erupted during the 1669 eruption are frequently attributed to long residence times, typical of 17th century activity at Mt. Etna (Viccaro et al., 2016; Magee et al., 2020). Indeed, estimated crystal residence times associated with the growth of Cr-rich mantles are longer (22 ± 2 days; Magee et al., 2020) than those from recent activity (6 ± 4 days for eruptions from 1974 to 2014; Ubide and Kamber, 2018). Our results indicate that decreasing crystal width and shorter residence times are associated with stronger sector enrichments for HFSE and REE, from 1669 megacrysts to 2002-03 phenocrysts and 1974 microphenocrysts. Below, we explore the relationship between ΔT, growth rates and residence time. We quantify ΔT and discuss implications for magma recharge, mush remobilisation and the onset of magma ascent along distinct pathways.

4.2. Quantifying magma undercooling

Magma undercooling exerts a significant control on the final composition and texture of clinopyroxene crystals (Kouchi et al., 1983; Mollo and Hammer, 2017; Masotta et al., 2020; MacDonald et al., 2022). As we note previously, the degree of sector enrichment in our crystals appears to be related to crystal growth rate and in turn to residence time and ΔT (Pontesilli et al., 2019; Moschini et al., 2021). Here, we use the ΔT model based on REE clinopyroxene-melt partitioning calibrated by MacDonald et al. (2022) to quantify magma ΔT associated with Cr-rich mantle zones. We calculate ΔT based on hourglass compositions, as the preferential uptake of REE in prism sectors leads to erroneously high ΔT (MacDonald et

al., 2022). The model calibration dataset uses experimental crystals synthesised from a mafic Etna trachybasalt composition (MacDonald et al., 2022), applicable to crystals from the 1974 and 2002-03 eruptions. Although the 1669 lavas are trachybasalts and have compositions similar to those produced experimentally for the REE model (Fig. S2b), clinopyroxene compositions deviate slightly from the general Etna trend (Fig. 3), and protracted crystal growth and storage attributed to megacrysts (Magee et al., 2021) and complicates the identification of an appropriate liquid composition to calculate apparent partition coefficients. Additionally, the crystals used to produce the REE calibration are considerably smaller (250 µm width for sector-zoned crystals) than megacrysts, highlighting that this model is likely not suitable the presumably lower ΔT related to megacrysts at Mt. Etna. Calculated ΔT for the 1974 crystals were previously reported in MacDonald et al. (2022), where REE apparent partition coefficients were determined by using a hand-picked groundmass composition for the melt (Magee et al., 2021). For the 2002-03 eccentric and central conduit melt compositions, we use the handpicked groundmass compositions (eccentric: 15-TU-106, central conduit: 16-SF-212) by Magee et al. (2021). Melt compositions and apparent partition coefficients are reported in Table S8. Prior to calculating ΔT, we test whether the apparent partition coefficients are indicative of near-equilibrium crystallisation conditions by the attainment of a local thermodynamic equilibrium at the crystal-melt interface. Following the guidelines set out by MacDonald et al. (2022), we plot Onuma curves for apparent partition coefficients from hourglass sectors to ensure that the uptake of REE into the M2 site of clinopyroxene follows thermodynamic principles for the partitioning energetics of trace cation substitutions (Onuma et al., 1968; Brice, 1975; Blundy and Wood, 1994). The logarithm of apparent partition coefficients from the 1974 and 2002-03 eruptions shows near-parabolic relationships with cation ionic radius, as the lattice strain energy exerts an overarching control on REE incorporation into the lattice site (Fig. S5). This excludes strong

447 disequilibrium uptake of REE under conditions of high melt supersaturation (Mollo and
448 Hammer, 2017). Indeed, near-equilibrium crystallisation conditions agree with the polyhedral
449 morphology of clinopyroxene in our samples (Fig. S1).
450 On average, our ΔT estimates are below the threshold for sector-zoned clinopyroxene
451 determined by experimental studies (ΔT < 45 °C; Kouchi et al., 1983, Masotta et al., 2020;
452 Fig. 7; Table S7). The average ΔT of all crystals fall within the model uncertainty (± 12 °C),
453 suggesting that conditions of mafic recharge may be similar regardless of eruption type. It is
454 important to note that this ΔT model is calibrated on compositions of clinopyroxene which
455 crystallised at ΔT ranging from 23 to 173 °C, with polyhedral, sector-zoned crystals formed at
456 the lower end of the ΔT range (ΔT = 23 – 32 °C) and higher undercoolings leading to skeletal
457 (ΔT = 75 – 123 °C) and dendritic (ΔT = 132 – 173 °C) crystals (MacDonald et al., 2022).
458 Hence, this calibration may not be sufficiently sensitive to distinguish between low and only
459 discreetly different ΔT. Despite this model limitation, inspection of ΔT kernel density
460 estimates does suggest that Cr-rich microphenocryst mantles from the 1974 eruption are
461 associated with slightly higher ΔT (ΔT = 41 ± 6 °C) than 2002-03 eccentric (ΔT = 31 ± 11 °C)
462 and central conduit (ΔT = 30 ± 6 °C) phenocryst mantles, which are almost indistinguishable
463 from one another (Fig. 7). The 1974 microphenocrysts show highest sector enrichments for
464 both ^{T}Al (Fig. 4) and trace elements (Fig. 5), suggesting they may have indeed crystallised
465 under the effect of more dynamic mafic recharge, mush remobilisation and onset of ascent
466 relative to 2002-03 phenocrysts. For comparison, we also calculate ΔT using the
467 clinopyroxene-only major element calibration of Masotta et al., (2020), based on the same
468 series of experiments but without the requirement of a representative equilibrium melt
469 composition, which is a limitation of the REE partitioning model by MacDonald et al., (2022;
470 Fig. 7). Results from the clinopyroxene major element model are within model uncertainty (±
471 22°C) of each other for our data set. However, phenocrysts from the 2002-03 eccentric

eruption typically return lower ΔT (41 ± 16 °C) than microphenocrysts from the 1974 eccentric eruption (ΔT = 47 ± 19 °C), similar to the results obtained using the REE clinopyroxene-melt partitioning model (Fig. 7). We note that both ΔT models are calibrated on single bulk compositions (Fig. S2a), limiting their application to other volcanic systems, yet return adequate results across our data set.

There are remarkably minimal differences in sector zoning between phenocryst mantles from the eccentric and central conduit 2002-03 eruptions. The similarity in ΔT estimates (Fig. 7) and sectoral enrichments of trace cations (Fig. 5) suggest that crystallisation of mantle zones and formation of sector zoning occurred under comparable conditions. Thus, clinopyroxene phenocrysts were recycled from compositionally similar mushes, regardless of final ascent pathway, with the main difference being the commonality of sector-zoned crystals in eccentric samples relative to their rarity in central conduit samples, which attests to the higher complexity of magma ascent through central conduits at Mt. Etna (Ubide and Kamber, 2018; Magee et al., 2021). If this interpretation is correct, then the outermost Cr-poor rim, crystallised upon ascent (Ubide and Kamber, 2018) may hold differences between eruption pathways, with central conduit ascent linked to lower ΔT than eccentric ascent.

Unfortunately, most clinopyroxene phenocrysts from the 2002-03 eccentric eruption have minimally developed Cr-poor outermost rims (< 35 μm in prism sectors), too thin for reliable data from both hourglass and prism sectors to be extracted. In contrast, rims from the 2002-03 central conduit eruptions can be much larger (> 84 μm in prism sectors) and in some cases, entire phenocrysts are Cr-poor (Fig. S4), as expected from limited sampling of mafic intrusions at depth due to more complex connections between magma reservoirs and longer crystal residence times relative to eccentric eruptions (Kahl et al., 2015).

Finally, we explore the relationship between ΔT estimates based on REE partitioning and concentrations in other trace elements in hourglass zones (Fig. 8). Experimental studies

497 highlight the link between ΔT and REE + HFSE in clinopyroxene, whilst low charge cations
498 such as large ion lithophile elements (LILE) are relatively unaffected (Mollo et al., 2013;
499 MacDonald et al., 2022). Hence, it would be expected that for natural crystals, ΔT should
500 only be weakly related to cations with low ionic potential and correlated with those with high
501 ionic potential. Following this, the concentration of monovalent cations such as Li is
502 unrelated to ΔT estimates (Fig. 8). Transition metals with low ionic potential and high crystal
503 field stabilisation energy such as Cr are also relatively unaffected by ΔT, further reinforcing
504 its low sensitivity to crystallisation kinetics. In contrast, HFSE are positively correlated with
505 ΔT, validating our proposal that the enrichment of cations with high ionic potential in prism
506 relative to hourglass sectors can be used to track ΔT and therefore the dynamic crystallisation
507 histories of magma, consistent with similar incorporation mechanisms governing the uptake
508 of both HFSE and REE in clinopyroxene from different eruptions at Mt. Etna. Minor
509 deviations from the correlation between ΔT and Ta (Fig. 8) are likely due to the analytical
510 limitations associated with measuring the naturally low concentration of Ta in clinopyroxene.
511 Further work combining ΔT estimates and sector enrichment, in conjunction with other tools
512 such as crystal size distributions (Moschini et al., 2021) may be pivotal in further unravelling
513 magma dynamics associated with magma recharge and ascent.

514 **4.3 Implications for magma dynamics**

515 Our work shows that the degree of sector enrichment in clinopyroxene reflects variations in
516 magma undercooling and may provide insights into pre-eruptive dynamics associated with
517 magma storage, mixing, mush disaggregation and the onset of ascent in alkaline systems.
518 Here, we link our results with pre-eruptive dynamics for each eruption to highlight the
519 potential of exploring sector zoning as a recorder of magmatic processes and discuss
520 implications for other volcanic settings and magma chemistries.
521 We first consider the 1669 flank eruption, the most voluminous and destructive in recorded

history at Mt. Etna, which heralded the conclusion of the 17th century eruption period, characterised by high effusion rates and long-lived volcanic activity (Condomines et al., 1995; Corsaro et al., 1996; Branca et al., 2013). Clinopyroxene megacrysts from the 1669 eruption exhibit weaker sector zoning in Cr-rich mantles than phenocrysts and microphenocrysts from recent eruptions (Fig. 5), possibly reflecting longer residence times in a crystallisation regime where growth was preferred over nucleation (low ΔT). Growth under initially high ΔT followed by prolonged storage can be discounted as these crystals do not exhibit textures indicative of initial growth under diffusion-controlled regimes (i.e., skeleton-overgrowth textures; Pontesilli et al., 2019). The high effusion rate of 17th century activity at Mt. Etna has been attributed to the development of long-lived magma reservoirs leading to protracted crystal growth in comparison to recent activity (Armienti et al., 1997; Viccaro et al., 2016). Cr-rich mantles in 1669 clinopyroxene are interpreted as recorders of eruption triggering 'cryptic' recharge (Magee et al., 2020). Sustained magma flux can lead to the crystallisation of megacrysts in volcanic systems (Landi et al., 2019), and mildly sector-zoned clinopyroxene megacrysts from Stromboli are interpreted to record protrated storage and convection at the edges of melt-dominated magmatic reservoirs, inducing low ΔT (Ubide et al., 2019b). Indeed, stirring experiments show convective mixing can enhance clinopyroxene crystallisation and limit kinetic effects, such as the development of sector zoning (Di Fiore et al., 2021). Hence, crystallisation of 1669 Cr-rich mantles may have taken place under conditions of low ΔT, where convection enhanced crystal growth and diminished the extent of sector zoning.

Recent (post 1970) activity at Mt. Etna is more closely associated with a 'steady-state' plumbing system with more frequent eruptions, smaller erupted volumes and shorter crystal residence times (Behncke and Neri, 2003; Clocchiatti et al., 2004; Viccaro et al., 2016). Reflecting this, the magnitude of sector enrichment in clinopyroxene microphenocrysts and

phenocrysts from the 1974 and 2002-03 eruptions, respectively, indicates that these Cr-rich mantles crystallised under higher ΔT conditions than those of Cr-rich mantles in megacrysts from the 1669 eruption (Fig. 5). We infer that the stronger sector zoning of Cr-rich mantles in the phenocrysts and microphenocrysts indicates processes of mush disaggregation by magma recharge events triggering the onset of magma ascent. Comparison of the two eruptions also reveals interesting, albeit subtle distinctions (Fig. 7). The 1974 microphenocrysts record slightly higher sector enrichment and ΔT, suggestive of more rapid recharge, mush remobilisation and initiation of ascent compared to the 2002-03 phenocrysts. Ten days prior to the 1974 eruption, Mt. Etna experienced its most intense seismic crisis recorded (Bottari et al., 1975), which has been interpreted to signify the intrusion of eruption triggering mafic magma (Corsaro et al., 2009; Ubide and Kamber, 2018). In contrast, the 2002-03 eruption was preceded by longer (8 weeks) and relatively less intense seismicity (Gambino et al., 2004). In line with this, clinopyroxene growth timescales are longer in 2002-03 relative to 1974 crystals (Ubide and Kamer 2018), and diffusion chronometry in olivine, constrains mafic recharge prior to the 2002-03 eruption at 44 ± 22 days (Kahl et al., 2015). The longer time between recharge and eruption for the 2002-03 products is consistent with slightly lower ΔT and hence larger crystal sizes and weaker sector enrichment of Cr-rich mantles compared to 1974 products, which document vigorous mixing and fast remobilisation to ascent with limited storage.

4.4. The role of melt geochemistry and magma undercooling on sector zoning across magmatic settings and compositions

More generally, sector zoning in clinopyroxene has been identified across a range of volcanic settings, including mid ocean ridges (Neave et al., 2019), arcs (Arculus, 1973; Brophy et al., 1999; Ubide et al., 2019b), continental hotspots (Tapu et al., 2022), oceanic hotspots (Ubide

et al., 2023), and in post-collisional systems (Zhou et al., 2021). Sector zoning may be broadly split by geochemical affinity; in tholeiitic systems, Na and Ca may also be preferentially incorporated into prism sectors alongside Al + Ti (Nakamura, 1973; Neave and Putirka, 2017; Neave et al., 2019), whereas in alkaline settings, Ca and Na are not strongly distributed between sectors (Ubide et al., 2019a, 2019b). To test the degree of sector enrichment as a recorder of dynamic pre-eruptive histories, and the potential effect of variations in melt composition on sector zoning across alkaline systems, we examine sector enrichment of ^{T}Al in clinopyroxene phenocryst from the 2021 eruption at Cumbre Vieja (La Palma, Canary Island ocean island basalts) published in Ubide et al (2023) and megacrysts from Roman era activity (2.4 – 1.8 ka; "Pizzo activity") at Stromboli volcano (data from Ubide et al., 2019b; Table S9; Fig. 9).

Throughout the duration of the Cumbre Vieja eruption, tephrite to basanite lavas were produced from the main fissure (termed "central cone" here). Toward the end of the eruption, basanite lavas were also produced episodically from fissures located several kilometres away from the central cone, which are termed "eccentric" by Ubide et al. (2023). Clinopyroxene from the 2021 La Palma eruption contain ubiquitous 'inner rims' (equivalent to our 'mantles'), which are sector-zoned and enriched in Cr_2O_3 and Mg# relative to neighbouring crystal zones, recording the onset of eruption triggering mafic recharge and mush disaggregation at upper mantle depths (Ubide et al., 2023). Similarly, Stromboli clinopyroxene megacrysts erupted from the Pizzo shoshonite scoria cone in Roman times, are comprised of Cr-rich mantle zones which transect hourglass and prism sectors (Ubide et al., 2019b). Both studies provide compositional data that are texturally constrained in respect to both oscillatory and sector zoning, affording a direct comparison with our Mt. Etna data.

In line with changes in melt chemistry (Fig. 9a), hourglass and prism sectors contain the highest ^{T}Al in clinopyroxene crystals from La Palma, followed by Mt. Etna, and finally,

Stromboli (Fig. 9b-d). We use matrix data as representative of eruption melt, instead of whole rock data which can be variably affected by phenocryst accumulation (Magee et al., 2022; Ubide et al., 2023; Fig. 7a). La Palma melts are more alkaline and SiO_2 undersaturated than Etna and Stromboli melts, likely modulating ^{T}Al. Alternatively, Al may be more preferentially incorporated into clinopyroxene at increasing pressures (Müntener et al., 2001), however, crystallisation pressures of Cr-rich clinopyroxene mantles are similar for La Palma (529 ± 150 MPa; Ubide et al., 2023), Mt. Etna (e.g., 1669 megacrysts between 400 – 500 MPa; Magee et al., 2020) and Stromboli (316 ± 33 MPa; Ubide et al., 2019b), therefore our data suggests that melt composition (i.e., increasing alkalinity) plays a major role on clinopyroxene ^{T}Al. On the other hand, sector enrichment (e.g., Δ^{T}Al) does not appear to be as strongly influenced by crystallisation pressure or melt composition and may provide a reliable indication of ΔT across different magmatic settings, as we explore below. Sector enrichment is comparable for crystal size populations between different alkaline systems (Fig. 9b). Megacrysts from Stromboli have the same Δ^{T}Al as megacrysts from the 1669 eruption at Mt. Etna, attesting to the limited development of sector zoning and consistent with protracted residence times (e.g., Ubide et al., 2019b). Similarly, phenocrysts from La Palma have Δ^{T}Al comparable to phenocrysts and microphenocrysts from Mt. Etna (Fig. 9b), suggestive of growth associated with mush remobilisation and the onset of ascent at $\Delta T < 45$ °C. Comparison of central and eccentric products from La Palma reveal that ^{T}Al between hourglass and prism sectors only differ by a minor amount (Δ^{T}Al = 0.08 for eccentric, Δ^{T}Al = 0.11 for central), highlighting that similar to the 2002-03 eccentric and central conduit eruptions at Mt. Etna, pre-eruptive mush dynamics associated with eruption-triggering mafic recharge are similar across eruption pathways and imply a degree of connectivity in pre-eruptive storage. We note that the number of samples for the eccentric fissure are low relative to the main cone (Fig. 9b), and postulate that this may reflect the slight differences in ^{T}Al we

observe.

Overall, our assessment highlights that across different mafic alkaline settings (i.e., arc and ocean island basalt), the development of sector zoning in phenocrysts and microphenocrysts is similar. This highlights that although ^{T}Al may be influenced by variations in melt compositions across alkaline systems, the development of sector zoning is seemingly unrelated. We stress that for subalkaline compositions, different incorporation mechanisms may be associated with sector zoning (Neave and Putirka 2017; Neave et al., 2019), and further investigations of sector-zoned clinopyroxene from these systems are required to explore this effect. Overall, this suggests the framework used here could be applied as a tool to investigate pre-eruptive magma dynamics at other volcanic systems. Further improvements of the geochemical inventory of texturally constrained sector-zoned clinopyroxene, experimental constraints, and application of this approach to natural systems may reveal further insights into pre-eruptive dynamics across other volcanic environments.

5. Conclusions

Using major, minor and trace element compositional variations between hourglass and prism sectors in clinopyroxene from a range of eruption types at Mt. Etna, we outline that sector zoning associated with Cr-rich mantle zones provides a detailed record of crystallisation kinetics. Across our entire range of crystal sizes, rare earth elements and high field strength elements are enriched alongside tetrahedral aluminium in prism sectors relative to simultaneously growing hourglass sectors. On the other hand, cations with low charge to ionic radius ratios, such as the large ion lithophile elements, and transition metal cations (e.g., Cr), are relatively unaffected by the development of sector zoning.

The degree of sector enrichment of cations varies with the degree of undercooling. In our samples, sector enrichment is highest for microphenocrysts from the 1974 eccentric eruption,

followed by phenocrysts from the 2002-03 eccentric and central conduit eruptions, and lowest for megacrysts from the 1669 flank (central conduit) eruption. We infer that variable crystal sizes across these eruptions reflect differences in crystal growth rates, magma undercooling and residence times, causing a systematic decrease in the development of sector zoning with crystal size. Quantification of undercooling, using clinopyroxene major elements and a REE partitioning, highlights that magma undercooling associated with magma recharge is similar across eruptions (ΔT < 45 °C). However, the combination of undercooling estimates and sectoral enrichment indicates that magma recharge, mush remobilisation and the initiation of magma ascent recorded by 1974 eccentric microphenocrysts was likely associated with higher undercooling than the 2002-03 phenocryst archives, confirming that higher degrees of sectoral enrichment are likely a reflection of increased magma undercooling. Undercooling and sector zoning are remarkably similar between crystals erupted from the eccentric and central conduit eruptions in 2002-03 at Mt. Etna, attesting to similar conditions of magma recharge and connectivity of mushes across eruption styles. Integrating our results to explore pre-eruptive dynamics in the 1669, 1974 and 2002-03 eruptions, we propose that variable sector enrichment of tetrahedral aluminium, high field strength elements and rare earth elements reflect differences in the dynamics of magmatic environments, including time from recharge to eruption. Comparison with sector-zoned Cr-rich zones from the 2021 La Palma eruption and from 2.4 – 1.8 ka Pizzo activity at Stromboli volcano highlights that sector enrichment varies as a function of crystal size and magma undercooling across different mafic alkaline settings. Importantly, sector partitioning does not appear to be influenced by variations in melt geochemistry, which does modulate mineral compositions. Overall, our approach indicates the potential of using the development of sector zoning in clinopyroxene to explore magma undercooling and pre-eruptive dynamics in active volcanic settings.

Acknowledgments

This work was supported by a Foundation Research Excellence Award from The University of Queensland, the Advance Queensland Women's Research Assistance Program from the Queensland Government and an Australian Research Council Discovery Project to T.U. (UQ-FREA RM2019001828, WRAP109-2019RD1 RM2020002371, ARC DP200101566). A.M. was supported by the Australian Government Research Training Program (RTP; PhD scholarship) for the duration of this study. S.M. was supported by "MIUR-PRIN 2022 PROVES Project (Grant #2022N4FBAA). We thank Henrietta Cathey for assistance with microprobe analysis at QUT and Jack Ward for support with LA-ICP-MS analysis at UQ. We also thank Jon Blundy and Penny Weiser for their comments and insights. Jinsheng Zhou, Charles D. Beard, and one anonymous reviewer are thanked for their thoughtful comments that materially improved the presentation and discussion of our results. We are very grateful to Rosemary Hickey-Vargas and Jeffrey Catalano for their helpful guidance as associate editor and executive editor of this journal.

Data Availability

Data are available through Mendeley Data at doi: 10.17632/bhtk35hgxz.3

Appendix A. Supplementary Material

The supplementary figures associated with this paper include photomicrographs and back scattered electron images of clinopyroxene crystals, groundmass and clinopyroxene classification diagrams, additional clinopyroxene LA-ICP-MS compositional maps for Cr and Onuma curves produced for all clinopyroxene crystals, provided in a single PDF file.

References

692 Andronico D., Branca S., Calvari S., Burton M., Caltabiano T., Corsaro R. A., Del Carlo P.,
693 Garfì G., Lodato L. and Miraglia L. (2005) A multi-disciplinary study of the 2002–03
694 Etna eruption: Insights into a complex plumbing system. *Bull. Volcanol.* **67**, 314-330.
695 Arculus R. J. (1973) *The alkali basalt andesite association of grenada lesser antilles* PhD
696 Thesis. Durham University.
697 Armienti P., Pareschi M. and Pompilio M. (1997) Lava textures and time scales of magma
698 storage at Mt. Etna (Italy). *Acta Vulcan.* **9**, 1-6.
699 Armienti P., Tonarini S., Innocenti F. and D Orazio M. (2007) Mount Etna pyroxene as tracer
700 of petrogenetic processes and dynamics of the feeding system. *Geol. Soc. Am. Spec.*
701 *Pap.* **418**, 265-276.
702 Armienti P., Perinelli C. and Putirka K. D. (2013) A new model to estimate deep-level
703 magma ascent rates, with applications to Mt. Etna (Sicily, Italy). *J. Petrol.* **54**, 795-
704 813.
705 Beard C.D., van Hinsberg V.J., Stix J., Wilke M. (2019) Clinopyroxene/melt trace
706 element partitioning in sodic alkaline magmas. *J. Petrol*. **60**, 1797–1823.Bernard C., Estrade
707 G., Salvi S., Béziat D., Smith M. (2020) Alkali pyroxenes and
708 amphiboles: a window on rare earth elements and other high field strength
709 elements behavior through the magmatic-hydrothermal transition of
710 peralkaline granitic systems. *Contrib. Miner. Petrol.* **175**, 1–27.
711 Behncke B. and Neri M. (2003) The July–August 2001 eruption of Mt. Etna (Sicily). *Bull.*
712 *Volcanol.* **65**, 461-476.
713 Bergantz G., Schleicher J. and Burgisser A. (2015) Open-system dynamics and mixing in
714 magma mushes. *Nat. Geosci.* **8**, 793-796.
715 Blundy J. and Wood B. (1994) Prediction of crystal–melt partition coefficients from elastic
716 moduli. *Nature* **372**, 452-454.

717 Blundy J., Robinson J. and Wood B. (1998) Heavy REE are compatible in clinopyroxene on
718 the spinel lherzolite solidus. *Earth Planet. Sci. Lett.* **160**, 493-504.
719 Bottari A., Lo Giudice E., Patanè G., Romano R. and Sturiale C. (1975) L'eruzione etnea del
720 gennaio-marzo 1974. *Riv. Min. Sic* **154**, 175-199.
721 Branca S., De Beni E. and Proietti C. (2013) The large and destructive 1669 ad eruption at
722 etna volcano: Reconstruction of the lava flow field evolution and effusion rate trend.
723 *Bull. Volcanol.* **75**, 1-16.
724 Brice J. (1975) Some thermodynamic aspects of the growth of strained crystals. *J. Cryst.*
725 *Growth* **28**, 249-253.
726 Brophy J. G., Whittington C. S. and Park Y.-R. (1999) Sector-zoned augite megacrysts in
727 aleutian high alumina basalts: Implications for the conditions of basalt crystallization
728 and the generation of calc-alkaline series magmas. *Contrib. Mineral. Petrol.* **135**, 277-
729 290.
730 Cashman K. and Blundy J. (2013) Petrological cannibalism: The chemical and textural
731 consequences of incremental magma body growth. *Contrib. Mineral. Petrol.* **166**,
732 703-729.
733 Clocchiatti R., Condomines M., Guénot N. and Tanguy J.-C. (2004) Magma changes at
734 Mount Etna: The 2001 and 2002–2003 eruptions. *Earth Planet. Sci. Lett.* **226**, 397-
735 414.
736 Condomines M., Tanguy J.-C. and Michaud V. (1995) Magma dynamics at Mt Etna:
737 Constraints from U-Th-Ra-Pb radioactive disequilibria and Sr isotopes in historical
738 lavas. *Earth Planet. Sci. Lett.* **132**, 25-41.
739 Corsaro R., Métrich N., Allard P., Andronico D., Miraglia L. and Fourmentraux C. (2009)
740 The 1974 flank eruption of Mount Etna: An archetype for deep dike-fed eruptions at

741 basaltic volcanoes and a milestone in Etn''s recent history. *J.l of Geophys. Res.: Solid*
742 *Earth* **114**.
743 Corsaro R. A., Cristofolini R. and Patanè L. (1996) The 1669 eruption at Mount Etna:
744 Chronology, petrology and geochemistry, with inferences on the magma sources and
745 ascent mechanisms. *Bull. Volcanol.* **58**, 348-358.
746 Costa F., Shea T., Ubide T. (2020) Diffusion chronometry and the timescales of magmatic
747 processes. *Nature Rev. Earth & Enviro.* **1**, 201-214.
748 Di Fiore F., Mollo S., Vona A., MacDonald A., Ubide T., Nazzari M., Romano C. and
749 Scarlato P. (2021) Kinetic partitioning of major and trace cations between
750 clinopyroxene and phonotephritic melt under convective stirring conditions: New
751 insights into clinopyroxene sector zoning and concentric zoning. *Chem. Geol.*,
752 120531.
753 Di Stefano F., Mollo S., Ubide T., Petrone C. M., Caulfield J., Scarlato P., Nazzari M.,
754 Andronico D. and Del Bello E. (2020) Mush cannibalism and disruption recorded by
755 clinopyroxene phenocrysts at Stromboli volcano: New insights from recent 2003–
756 2017 activity. *Lithos* **360**, 105440.
757 Downes M. (1974) Sector and oscillatory zoning in calcic augites from Mt. Etna, Sicily.
758 *Contrib. Mineral. Petrol.* **47**, 187-196.
759 Dowty E. (1976) Crystal structure and crystal growth: II. Sector zoning in minerals. *Am.*
760 *Mineral.* **61**, 460-469.
761 Dowty E. (1980) Crystal growth and nucleation theory and the numerical simulation of
762 igneous crystallization. *Physics of Magmatic Processes*. Princeton Univ. Press. pp.
763 419-486.

764 Gambino S., Mostaccio A., Patanè D., Scarfì L. and Ursino A. (2004) High-precision
765 locations of the microseismicity preceding the 2002–2003 Mt. Etna eruption.
766 *Geophys. Res. Lett.* **31**.
767 Duncan A. M. & Preston R.M.F. (1980) Chemical variation of clinopyroxene phenocrysts
768 from the trachybasaltic lavas of Mount Etna, Sicily. *Min. Magazine.* **43**(330), 765-
769 770.
770 Giacomoni P. P., Coltorti M., Bryce J., Fahnestock M. and Guitreau M. (2016) Mt. Etna
771 plumbing system revealed by combined textural, compositional, and
772 thermobarometric studies in clinopyroxenes. *Contrib. Mineral. Petrol.* **171**, 34.
773 Grove T. L. and Bence A. Crystallization kinetics in a multiply saturated basalt magma-an
774 experimental study of luna 24 ferrobasalt. *Proc. Lunar Planet. Sci. Conf.*
775 Hill E., Wood B. J. and Blundy J. D. (2000) The effect of Ca-Tschermaks component on
776 trace element partitioning between clinopyroxene and silicate melt. *Lithos* **53**, 203-
777 215.
778 Hollister L. S. and Gancarz A. J. (1971) Conpositional sector-zoning in clinopyroxene from
779 the Narce area, Italy. *Am. Mineral.t***56**, 959-979.
780 Kahl M., Chakraborty S., Pompilio M. and Costa F. (2015) Constraints on the nature and
781 evolution of the magma plumbing system of Mt. Etna volcano (1991–2008) from a
782 combined thermodynamic and kinetic modelling of the compositional record of
783 minerals. *J. Petrol.* **56**, 2025-2068.
784 Kahl M., Viccaro M., Ubide T., Morgan D. J. and Dingwell D. B. (2017) A branched magma
785 feeder system during the 1669 eruption of Mt Etna: Evidence from a time-integrated
786 study of zoned olivine phenocryst populations. *J. Petrol.* **58**, 443-472.

787 Kouchi A., Sugawara Y., Kashima K. and Sunagawa I. (1983) Laboratory growth of sector
788 zoned clinopyroxenes in the system $CaMgSi_2O_6$-$CaTiAl_2O_6$. *Contrib. Mineral. Petrol.*
789 **83**, 177-184.
790 Landi P., La Felice S., Petrelli M., Vezzoli L. M. and Principe C. (2019) Deciphering textural
791 and chemical zoning of k-feldspar megacrysts from mt. Amiata volcano (southern
792 tuscany, italy): Insights into the petrogenesis and abnormal crystal growth. *Lithos* **324**,
793 569-583.
794 Leung I. S. (1974) Sector-zoned titanaugites: Morphology, crystal chemistry, and growth.
795 *Am. Mineral.t* **59**, 127-138.
796 Lofgren G. (1980) Experimental studies on the dynamic crystallization of silicate melts.
797 *Physics of Magmatic Processes*. Princeton Univ. Press 487-551MacDonald A., Ubide T.,
798 Mollo S., Masotta M. and Pontesilli A. (2022) Trace element partitioning in zoned
799 clinopyroxene as a proxy for undercooling: Experimental constraints from
800 trachybasaltic magmas. *Geochim. Cosmochim. Acta* **336**, 249-268.
801 Magee R., Ubide T. and Kahl M. (2020) The lead-up to Mount Etna's most destructive
802 historic eruption (1669). Cryptic recharge recorded in clinopyroxene. *J. Petrol.* **61**,
803 egaa025.
804 Magee R., Ubide T. and Caulfield J. (2021) Days to weeks of syn-eruptive magma
805 interaction: High-resolution geochemistry of the 2002-03 branched eruption at Mount
806 Etna. *Earth Planet. Sci. Lett.* **565**, 116904.
807 Masotta M., Pontesilli A., Mollo S., Armienti P., Ubide T., Nazzari M. and Scarlato P. (2020)
808 The role of undercooling during clinopyroxene growth in trachybasaltic magmas:
809 Insights on magma decompression and cooling at Mt. Etna volcano. *Geochim.*
810 *Cosmochim. Acta* **268**, 258-276.

Métrich N., Allard P., Spilliaert N., Andronico D. and Burton M. (2004) 2001 flank eruption of the alkali-and volatile-rich primitive basalt responsible for Mount Etna's evolution in the last three decades. *Earth Planet. Sci. Lett.* **228**, 1-17.

Mollo S., Blundy J., Iezzi G., Scarlato P. and Langone A. (2013) The partitioning of trace elements between clinopyroxene and trachybasaltic melt during rapid cooling and crystal growth. *Contrib. Mineral. Petrol.* **166**, 1633-1654.

Mollo S., Giacomoni P. P., Coltorti M., Ferlito C., Iezzi G. and Scarlato P. (2015) Reconstruction of magmatic variables governing recent etnean eruptions: Constraints from mineral chemistry and P–T–fo_2–H_2O modeling. *Lithos* **212**, 311-320.

Mollo S. and Hammer J. (2017) Dynamic crystallization in magmas. *EMU Notes Mineral* **16**, 373-418.

Mollo S., Blundy J., Scarlato P., De Cristofaro S. P., Tecchiato V., Di Stefano F., Vetere F., Holtz F. and Bachmann O. (2018) An integrated PT-H_2O-lattice strain model to quantify the role of clinopyroxene fractionation on REE+ Y and HFSE patterns of mafic alkaline magmas: Application to eruptions at Mt. Etna. *Earth-Science Reviews* **185**, 32-56.

Mollo S., Blundy J., Scarlato P., Vetere F., Holtz F., Bachmann O. and Gaeta M. (2020) A review of the lattice strain and electrostatic effects on trace element partitioning between clinopyroxene and melt: Applications to magmatic systems saturated with tschermak-rich clinopyroxenes. *Earth Sci. Rev.*, 103351.

Mollo S., Moschini P., Ubide T., MacDonald A., Vetere F., Nazzari M., Misiti V., Miyajima M., Melai C., Di Genova D., Vona A., Di Fiore F., and Romano C. (2023) Kinetic partitioning of trace cations between zoned clinopyroxene and a variably cooled-decompressed alkali basalt: Thermodynamic considerations on lattice strain and electrostatic energies of substitution. *Geochim. Cosmochim. Acta* **361**, 40–66.

836 Moschini P., Mollo S., Gaeta M., Fanara S., Nazzari M., Petrone C. M. and Scarlato P.
837 (2021) Parameterization of clinopyroxene growth kinetics via crystal size distribution
838 (csd) analysis: Insights into the temporal scales of magma dynamics at Mt. Etna
839 volcano. *Lithos* **396**, 106225.
840 Morimoto N. (1988) Nomenclature of Pyroxenes. *Min. and Petrol.* **39**, 59 – 76.
841 Mulas M., Cioni R., Andronico D. and Mundula F. (2016) The explosive activity of the 1669
842 monti rossi eruption at Mt. Etna (Italy). *J. Volcanol. Geotherm. Res.* **328**, 115-133.
843 Müller T., Dohmen R., Becker H., Ter Heege J. H. and Chakraborty S. (2013) Fe–mg
844 interdiffusion rates in clinopyroxene: Experimental data and implications for Fe–Mg
845 exchange geothermometers. *Contrib. Mineral. Petrol.* **166**, 1563-1576.
846 Müntener O., Kelemen P. B. and Grove T. L. (2001) The role of H2O during crystallization
847 of primitive arc magmas under uppermost mantle conditions and genesis of igneous
848 pyroxenites: An experimental study. *Contrib. Mineral. Petrol.* **141**, 643-658.
849 Nakamura Y. (1973) Origin of sector-zoning of igneous clinopyroxenes. *Am. Mineral.* **58**,
850 986-990.
851 Neave D. A., Maclennan J., Hartley M. E., Edmonds M. and Thordarson T. (2014) Crystal
852 storage and transfer in basaltic systems: The Skuggafjöll eruption, Iceland. *J. Petrol.*
853 **55**, 2311-2346.
854 Neave D. A. and Putirka K. D. (2017) A new clinopyroxene-liquid barometer, and
855 implications for magma storage pressures under icelandic rift zones. *Am. Mineral.*
856 **102**, 777-794.
857 Neave D. A., Bali E., Guðfinnsson G. H., Halldórsson S. A., Kahl M., Schmidt A.-S. and
858 Holtz F. (2019) Clinopyroxene–liquid equilibria and geothermobarometry in natural
859 and experimental tholeiites: The 2014–2015 Holuhraun eruption, Iceland. *J. Petrol.*
860 **60**, 1653-1680.

Onuma N., Higuchi H., Wakita H. and Nagasawa H. (1968) Trace element partition between two pyroxenes and the host lava. *Earth Planet. Sci. Lett.* **5**, 47-51.

Paton C., Hellstrom J., Paul B., Woodhead J. and Hergt J. (2011) Iolite: Freeware for the visualisation and processing of mass spectrometric data. *J. Anal. At. Spectrom.* **26**, 2508-2518.

Perinelli C., Mollo S., Gaeta M., De Cristofaro S. P., Palladino D. M., Armienti P., Scarlato P. and Putirka K. D. (2016) An improved clinopyroxene-based hygrometer for etnean magmas and implications for eruption triggering mechanisms. *Am. Mineral.* **101**, 2774-2777.

Petrus J., Chew D., Leybourne M. and Kamber B. (2017) A new approach to laser-ablation inductively-coupled-plasma mass-spectrometry (la-icp-ms) using the flexible map interrogation tool 'monocle'. *Chem. Geol.* **463**, 76-93.

Pontesilli A., Masotta M., Nazzari M., Mollo S., Armienti P., Scarlato P. and Brenna M. (2019) Crystallization kinetics of clinopyroxene and titanomagnetite growing from a trachybasaltic melt: New insights from isothermal time-series experiments. *Chem. Geol.* **510**, 113-129.

Pontesilli A., Brenna M., Ubide T., Mollo S., Masotta M., Caulfield J., Le Roux P., Nazzari M., Scott J. and Scarlato P. (2021) Intraplate basalt alkalinity modulated by a lithospheric mantle filter at the Dunedin volcano (New Zealand). *J. Petrol.* **62**, egab062.

Putirka K. D. (2008) Thermometers and barometers for volcanic systems. *Rev. Mineral. Geochem.* **69**, 61-120.

Ruth D. and Costa F. (2021) A petrological and conceptual model of mayon volcano (philippines) as an example of an open-vent volcano. *Bull. Volcanol.* **83**, 62.

885 Shannon R. D. (1976) Revised effective ionic radii and systematic studies of interatomic
886 distances in halides and chalcogenides. *Acta Crystallogr.***32**, 751-767.
887 Shea T. and Hammer J. E. (2013) Kinetics of cooling-and decompression-induced
888 crystallization in hydrous mafic-intermediate magmas. *J. Volcanol. Geotherm. Res.*
889 **260**, 127-145.
890 Shimizu N. (1981) Trace element incorporation into growing augite phenocryst. *Nature* **289**,
891 575-577.
892 Smith R. K. and Lofgren G. E. (1973) An analytical and experimental study of zoning in
893 plagioclase. *Lithos* **16** 153-168.
894 Streck M. J. (2008) Mineral textures and zoning as evidence for open system processes. *Rev.*
895 *Mineral. Geochem.* **69**, 595-622.
896 Tapu A., Ubide T. and Vasconcelos P. (2022) Plumbing system architecture of late-stage
897 hotspot volcanoes in eastern australia. *J. Petrol.* **63**, egac015.
898 Ubide T., McKenna C. A., Chew D. M. and Kamber B. S. (2015) High-resolution LA-ICP-
899 MS trace element mapping of igneous minerals: In search of magma histories. *Chem.*
900 *Geol.* **409**, 157-168.
901 Ubide T. and Kamber B. S. (2018) Volcanic crystals as time capsules of eruption history.
902 *Nature Commun.* **9**, 1-12.
903 Ubide T., Mollo S., Zhao J.-x., Nazzari M. and Scarlato P. (2019a) Sector-zoned
904 clinopyroxene as a recorder of magma history, eruption triggers, and ascent rates.
905 *Geochim. Cosmochim. Acta* **251**, 265-283.
906 Ubide T., Caulfield J., Brandt C., Bussweiler Y., Mollo S., Di Stefano F., Nazzari M. and
907 Scarlato P. (2019b) Deep magma storage revealed by multi-method elemental
908 mapping of clinopyroxene megacrysts at Stromboli volcano. *Front. Earth Sci.* **7**, 239.

Ubide T., Neave D. A., Petrelli M. and Longpré M.-A. (2021) Crystal archives of magmatic processes. *Front. Earth Sci.*, 722.

Ubide T., Márquez Á., Ancochea E., Huertas M. J., Herrera R., Coello-Bravo J. J., Sanz-Mangas D., Mulder J., MacDonald A. and Galindo I. (2023) Discrete magma injections drive the 2021 La Palma eruption. *Sci. Adv.* **9**

Van Orman J. A., Grove T. L. and Shimizu N. (2001) Rare earth element diffusion in diopside: Influence of temperature, pressure, and ionic radius, and an elastic model for diffusion in silicates. *Contrib. Mineral. Petrol.* **141**, 687-703.

Viccaro M., Barca D., Bohrson W. A., D'Oriano C., Giuffrida M., Nicotra E. and Pitcher B. W. (2016) Crystal residence times from trace element zoning in plagioclase reveal changes in magma transfer dynamics at Mt. Etna during the last 400 years. *Lithos* **248**, 309-323.

Wang Z.-C., Zhou M.-F., Li M. Y. H., Robinson P. T. and Harlov D. E. (2022) Kinetic controls on sc distribution in diopside and geochemical behavior of sc in magmatic systems. *Geochim. Cosmochim. Acta*.

Wood B. J. and Blundy J. D. (2001) The effect of cation charge on crystal–melt partitioning of trace elements. *Earth Planet. Sci. Lett.* **188**, 59-71.

Zhou, J.S., Wang, Q., Xing, C.M., Ma, L., Hao, L.L., Li, Q.W., Wang, Z.L. and Huang, T.Y. (2021) Crystal growth of clinopyroxene in mafic alkaline magmas. *Earth Planet. Sci. Lett.* **568**, 117005.

Figures

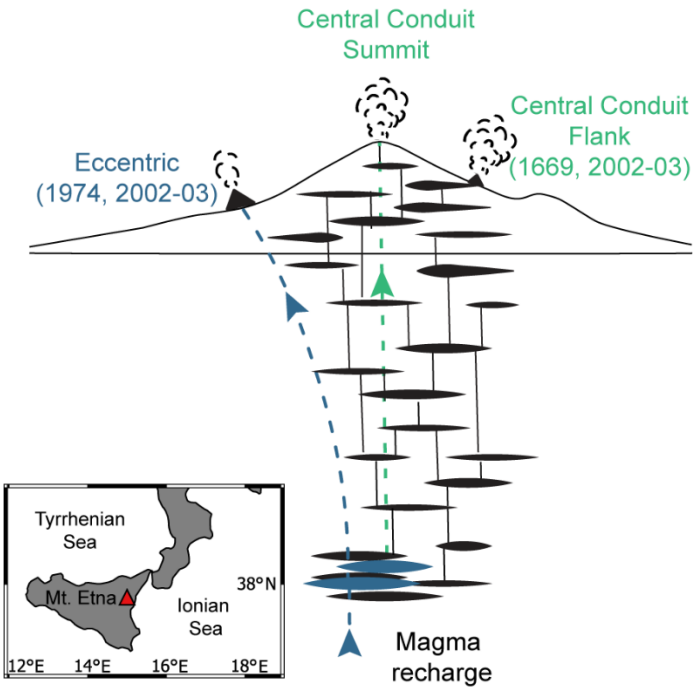

Fig. 1: Schematic illustration of magmatic pathways at Mt. Etna, Italy (redrawn after Ubide and Kamber, 2018) with eruptions studied in this work. Eccentric pathways are indicated in blue and bypass the central conduit system, indicated in green. All summit eruptions are fed by the vertically extended, complex central conduit plumbing system. Flank eruptions are often fed by the central conduits but can also feed from eccentric pathways, offering a more direct ascent pathways that may be conductive to high magma undercooling. Insert map shows the location of Mt. Etna on the island of Sicily, Italy.

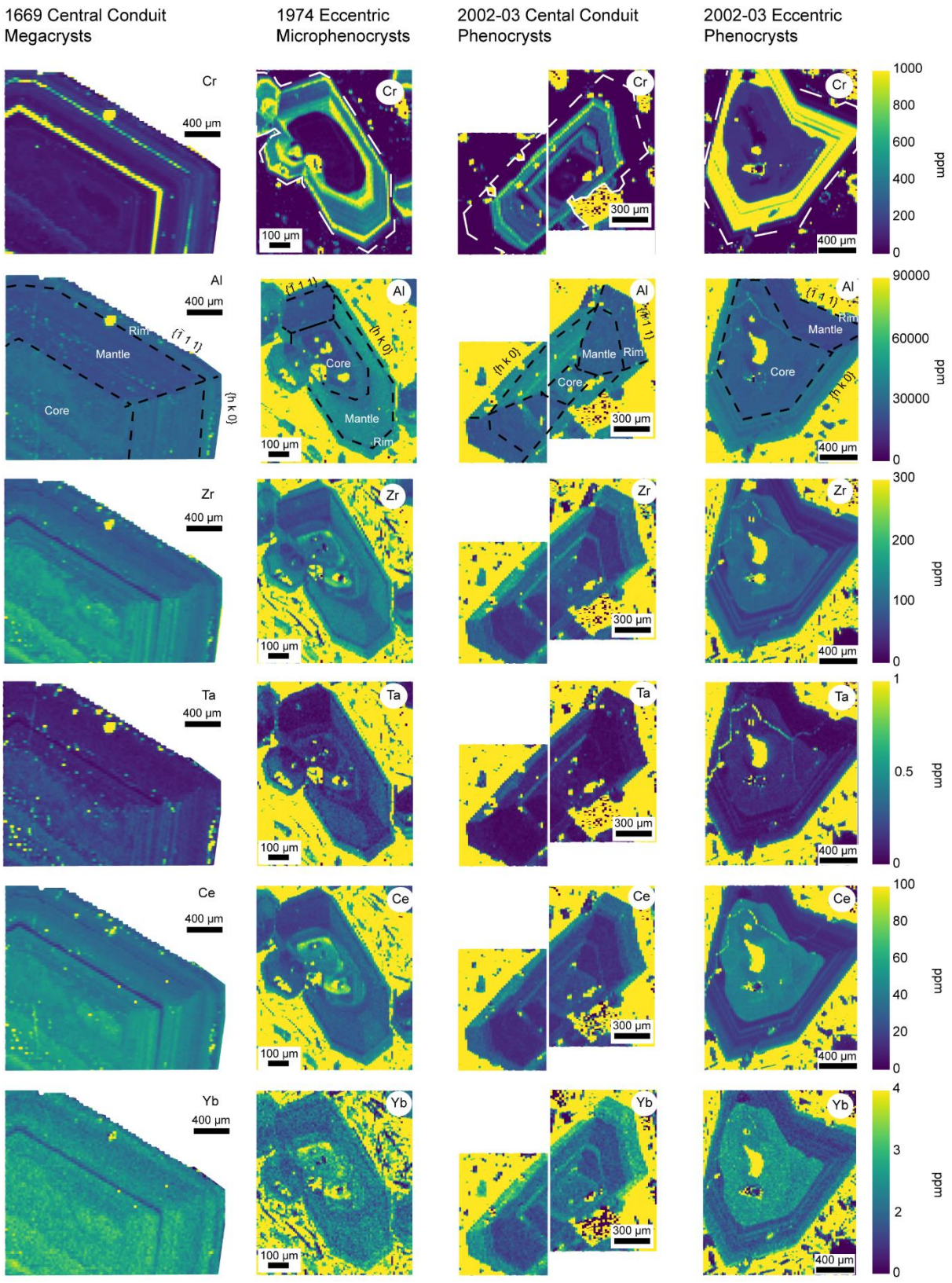

Fig. 2: LA-ICP-MS compositional maps of representative clinopyroxene crystals from the 1669, 1974 and 2002-03 eruptions at Mt. Etna, Italy. Crystal zones (core, mantle and rim) and

sectors (prism and hourglass) are marked for each crystal. White dashed lines on Cr maps indicate crystal edges. All crystals presented here record mafic recharge as indicated by Cr enrichments coupled with depletions in high field strength elements (e.g., Zr and Ta) and rare earth elements (e.g., Ce and Yb) (Ubide and Kamber, 2018). Data for the 1974 microphenocrysts are from Ubide et al. (2019b). Concentration scales are quantitative for clinopyroxene and semi-quantitative for other phases included in the maps (see Methods).

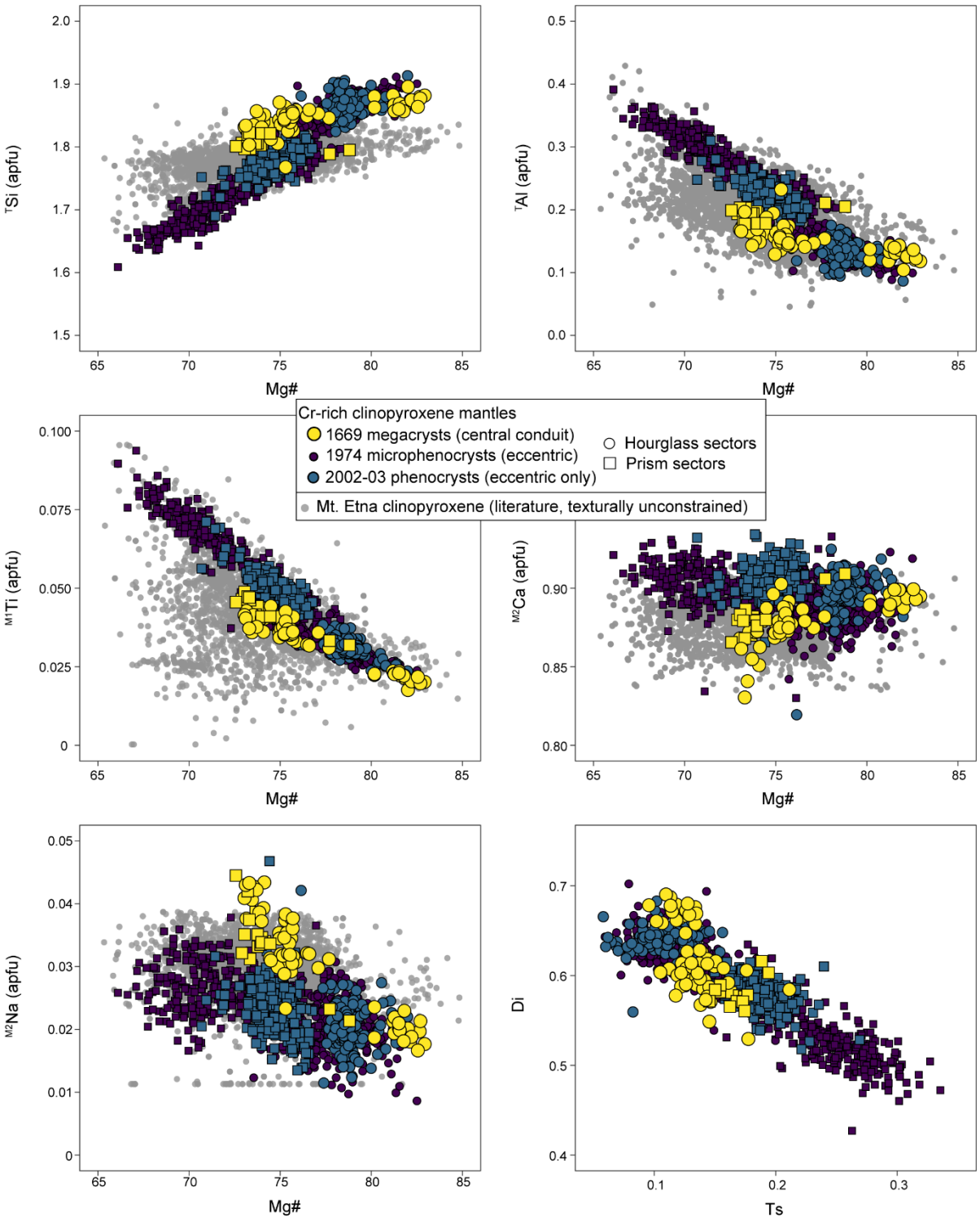

974

975 Fig. 3: Major and minor cation contents (in atoms per formula unit; apfu) plotted against Mg#
976 (MgO/MgO + FeO_t × 100 on molar basis) of sector-zoned mantles of clinopyroxene crystals
977 from the 1974 eccentric, 2002-03 eccentric and 1669 flank (central conduit) eruptions. Data
978 from 1974 and 2002-03 are from Ubide et al. (2019b). Light grey circles indicate

clinopyroxene literature data from GEOROC (https://georoc.eu/), obtained on 24/8/22 using the following parameters: geological setting = complex: volcanic settings = Etna/Sicily: mineral/component = augite/clinopyroxene: rock type = volcanic rock: type of material: mineral and was further filtered to only include clinopyroxene from trachybasalts (Table S5).

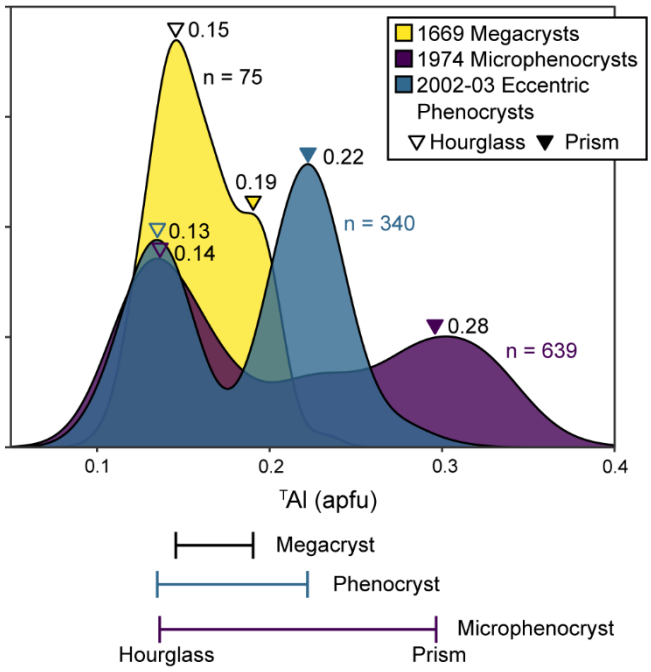

Fig. 4: Comparison of tetrahedral aluminium (^{T}Al) in Cr-rich mantle zones of clinopyroxene across different eruptions at Mt. Etna and crystal sizes as kernel density estimates. The average ^{T}Al content for hourglass and prism sectors for each population is marked below the plot, and highlights increasing enrichment in ^{T}Al in prism relative to hourglass sector with decreasing crystal size.

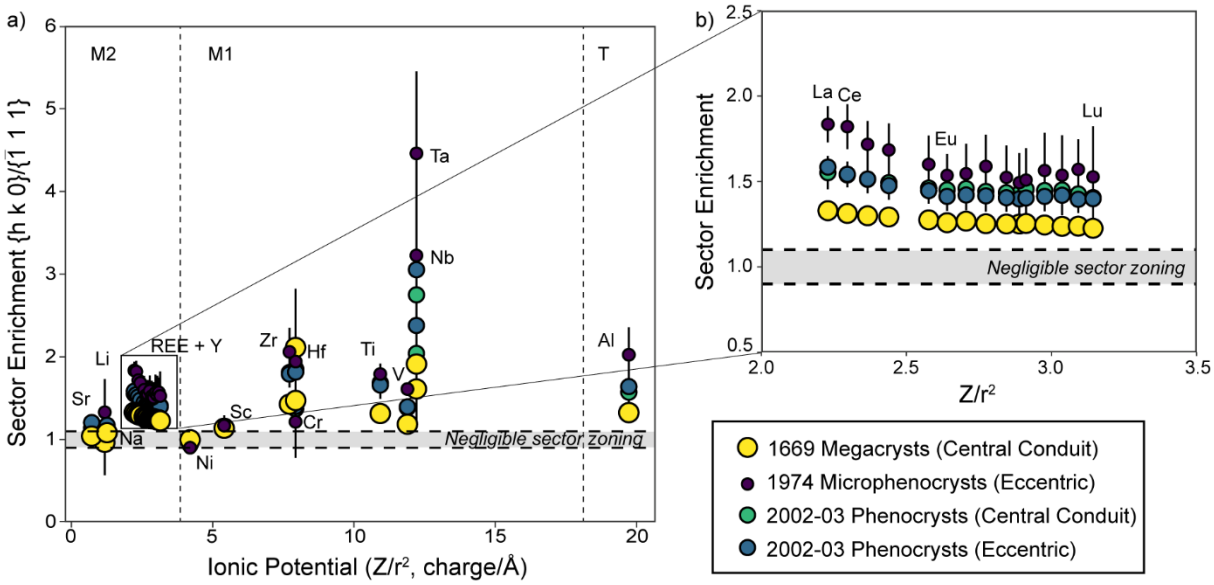

Fig. 5: a) Sector enrichment of minor and trace elements in clinopyroxene, calculated as the ratio between the concentration in prism sectors {*h k* 0} to hourglass sectors {- 1 1 1}, in Cr-rich mantle zones. Values are plotted as a function of ionic potential, which is the ratio of the charge of the cation (*Z*) and the square of the ionic radius (r^2), as proposed in Shimizu (1981) and applied to Mt. Etna in Ubide et al. (2019b). Cation radii are from Shannon (1976) in IV-fold (T site), VI-fold (M1 site) and VIII-fold (M2 site) coordinations. For Al, we only consider the radius for IV-fold coordination (tetrahedral site). Plotted values represent average sector enrichments for each eruption, and error bars represent one standard deviation. b) Sector enrichment of the isovalent series of REE series occupying the M2 site.

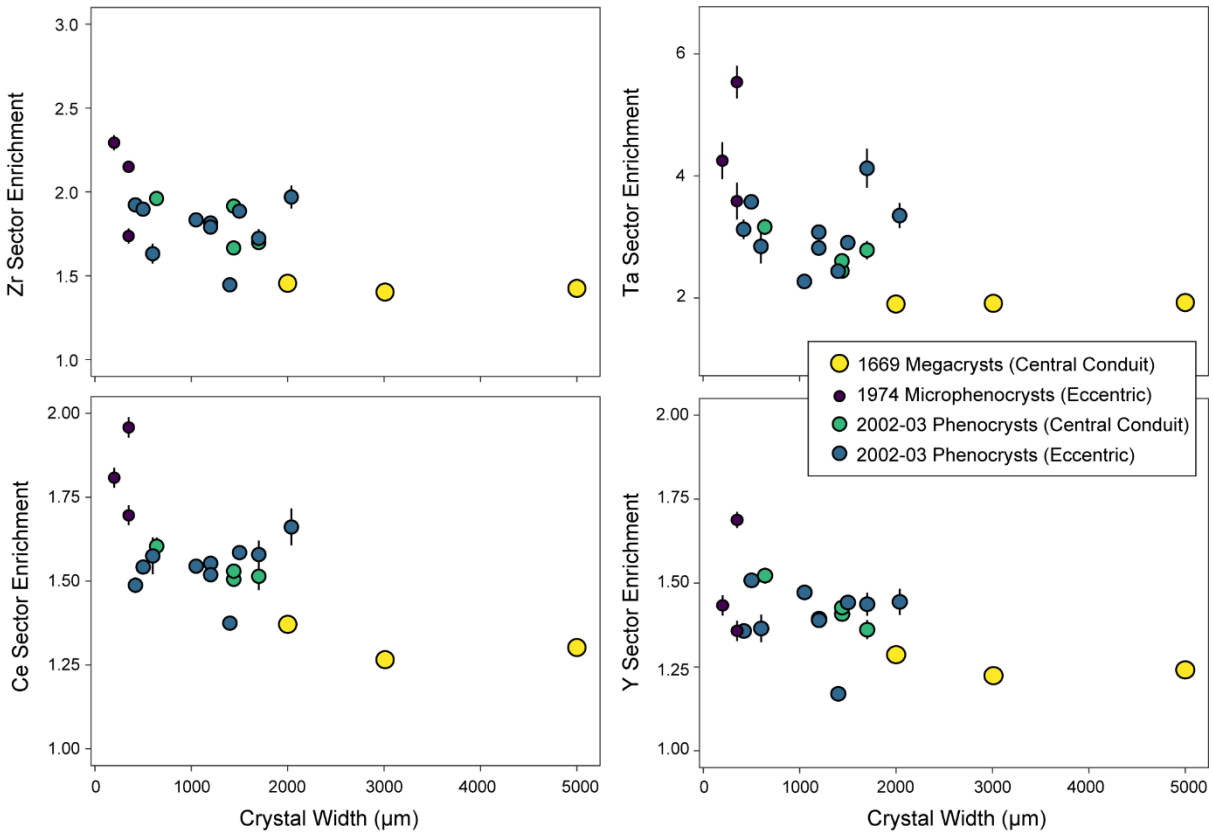

Fig. 6: Sector enrichment of selected HFSE (Zr, Ta) and REE (Ce, Y) as a function of crystal width. Uncertainties were propagated from 2 × standard errors from extracted LA-ICP-MS data. Sector enrichment increases with decreasing crystal width (increasing magma undercooling).

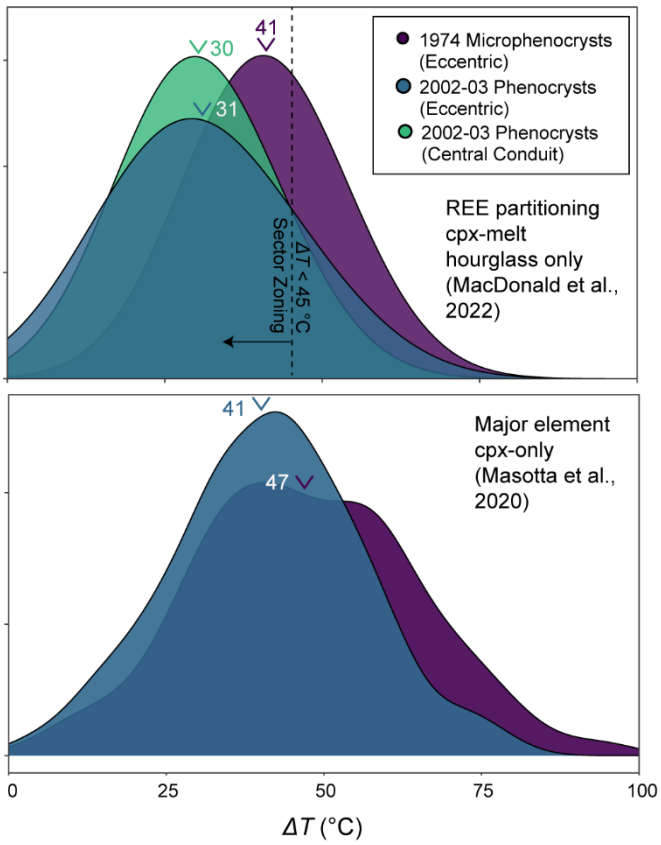

1022

1023 Fig. 7: Undercooling (ΔT) calculated using clinopyroxene-melt REE partition coefficients
1024 (MacDonald et al., 2022) from hourglass sectors of 1974 and 2002-03 clinopyroxene crystals,
1025 and using the clinopyroxene-only major element model of Masotta et al., (2020). As per
1026 previous figures, we only consider the Cr-rich mantle zones. The dashed line in the top plot
1027 represents the experimentally determined upper limit of ΔT for sector-zoned clinopyroxene
1028 (Kouchi et al., 1983; Masotta et al., 2020). Undercooling modelled from natural crystals
1029 agree with sector zoning developing at ΔT <45ºC, with microphenocrysts from the 1974
1030 eccentric eruption returning slightly higher undercooling than larger crystals from the
1031 eccentric and central conduit eruptions.

1032

1033

1034

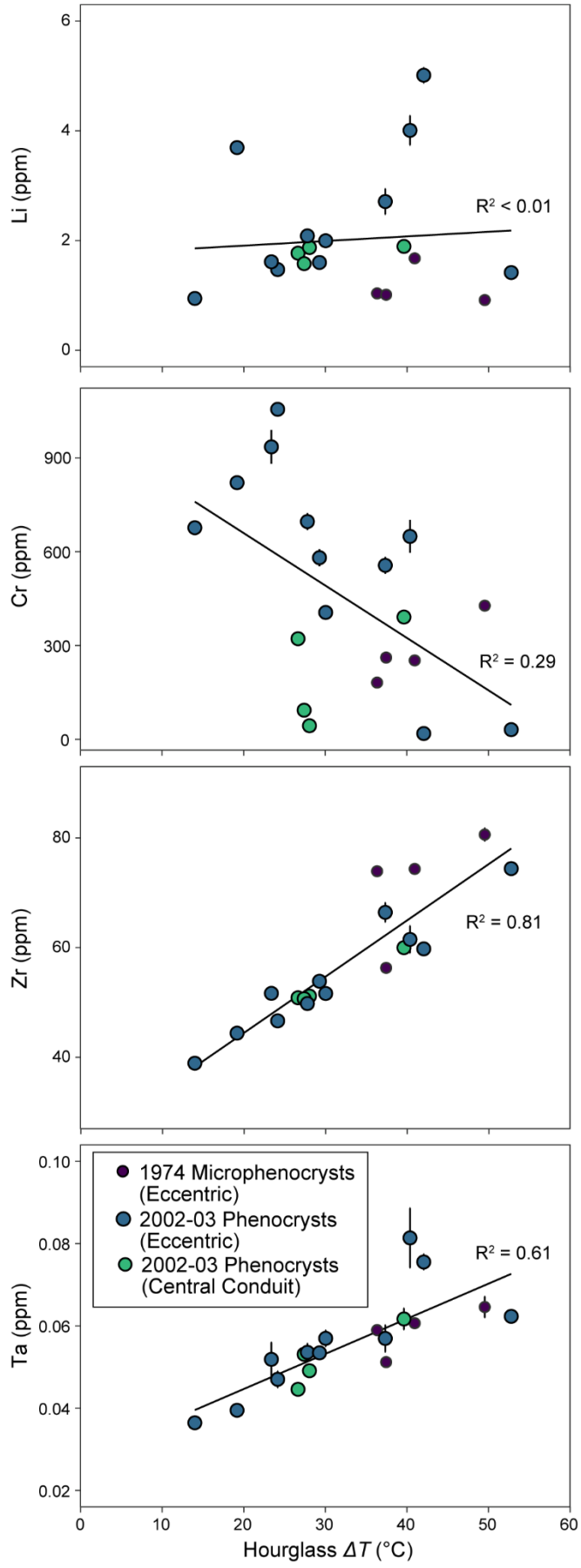
Li (ppm)
R² < 0.01
Cr (ppm)
R² = 0.29
Zr (ppm)
R² = 0.81
Ta (ppm)
R² = 0.61
1974 Microphenocrysts (Eccentric)
2002-03 Phenocrysts (Eccentric)
2002-03 Phenocrysts (Central Conduit)
Hourglass ΔT (°C)

1035

Fig. 8: Relationship between calculated ΔT and concentration of large ion lithophile elements (LILE; Li), transition metals (Cr) and high field strength elements (HFSE; Zr and Ta) in hourglass sectors of our clinopyroxene crystals. Simple linear regression yields variable coefficients of determination (R^2) across the range of examined elements. Only the HFSE define a clear positive correlation with ΔT, as expected from their dependence on charge balancing substitutions (Ubide et al., 2019a; MacDonald et al., 2022). Error bars represent 2 × standard error from data extracted from LA ICP-MS compositional maps.

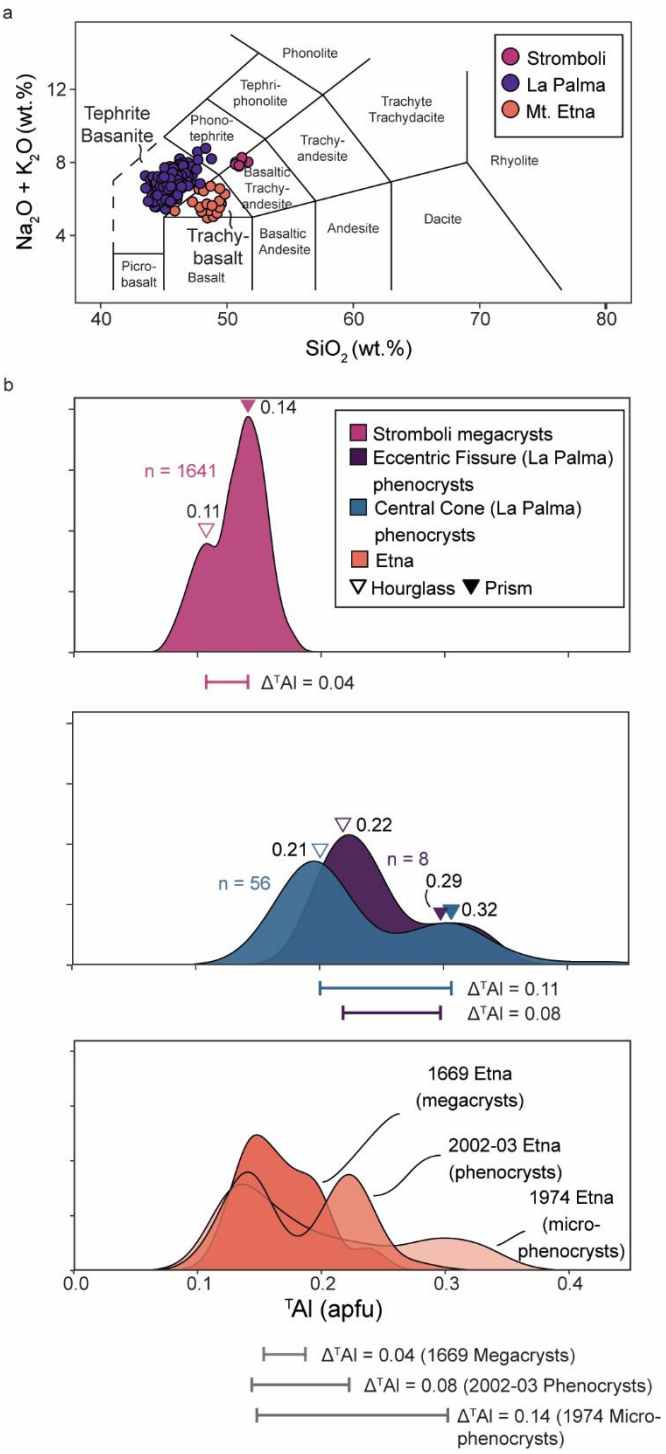

Fig. 9: a) Total Alkali Silica (TAS) diagram comparing matrix (microcrystalline groundmass) compositions from the 2021La Palma eruption, (ocean island basalt system, Canary Islands), the Roman era Pizzo activity at Stromboli volcano (Italy, arc), and the 1974 and 2002-03 eruptions at Mt. Etna (Italy). Data from the eruption at Cumbre Vieja are from Ubide et al. (2023), data from Stromboli are from Ubide et al. (2019b) and data from the Mt. Etna

eruptions are from Magee et al. (2020, 2021).

b) Kernel density estimates (KDE) of tetrahedral aluminium (^{T}Al) from hourglass and prism sectors of Cr-rich zones associated with eruption triggering magma recharge from clinopyroxene megacrysts from Stromboli Ubide et al. (2019b), La Palma (Ubide et al., 2023) and Etna (this study; full details of this plot are reported in Fig. 4). Average hourglass and prism ^{T}Al contents are indicated by empty and filled triangles, respectively. Difference between ^{T}Al content of hourglass and prism sectors are indicated by the bars below each plot. Melt composition modulates absolute Al concentrations in clinopyroxene, yet Al enrichment between sectors is independent of melt composition and modulated by magma dynamics, increasing with ΔT from microphenocrysts to phenocrysts to megacrysts across eruptions and magmatic compositions.

Supplementary Figure 1: a) Reflected light photomicrograph of a clinopyroxene (cpx) megacryst from the 1669 flank eruption mounted in resin, cut parallel to the c-axis of the crystal. As crystals were cut twice to achieve this mount, only half of the full crystal is mounted here. b) Transmitted light photomicrograph of a lava sample erupted during the 1974 eccentric eruption at Mt. Etna. Clinopyroxene and olivine (ol) are present as microphenocrysts and plagioclase (pl) is restricted to the groundmass. c – d) Transmitted light photomicrographs of samples from the 2002-03 eccentric (c) and central conduit (d) eruptions. Clinopyroxene and olivine phenocrysts are present in both samples. Plagioclase is more abundant as phenocrysts in the central conduit products, as previously described for this eruption (e.g., Magee et al., 2021).

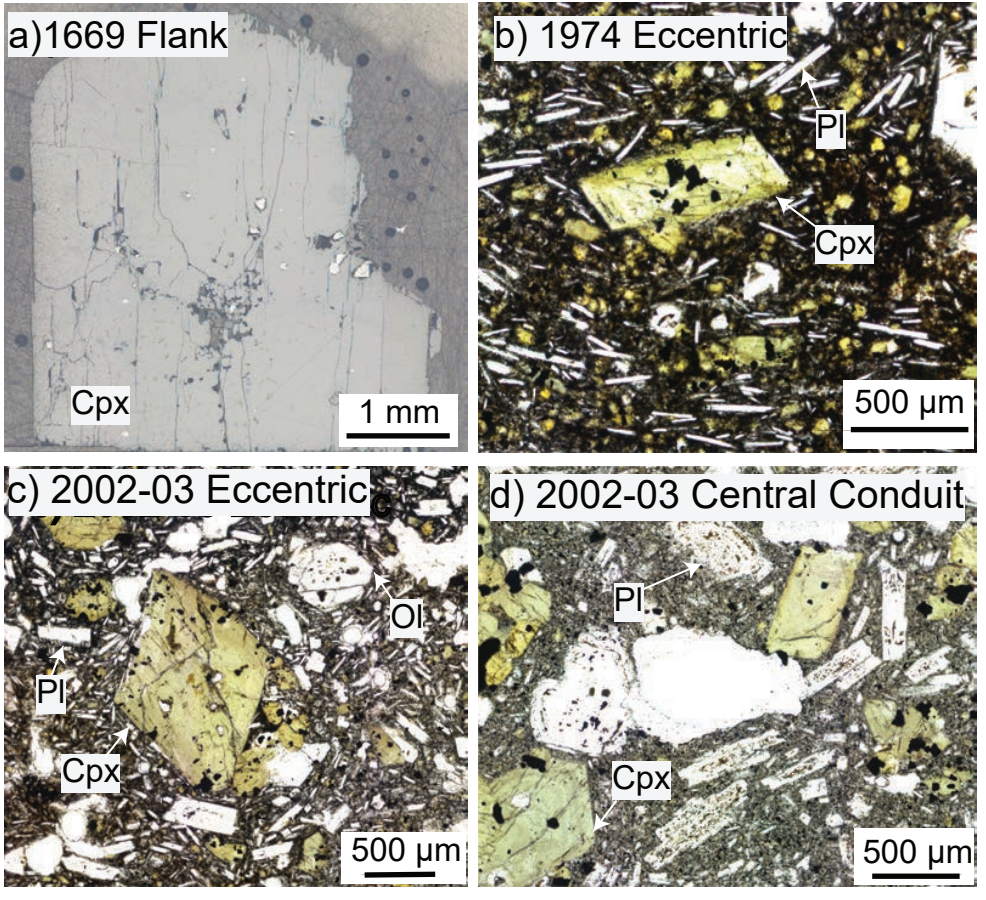

Supplementary Figure 2: a) Total alkali silica (TAS) diagram of groundmass compositions from the 1669 (Magee et al., 2020), 1974 eccentric and 2002-03 central conduit and eccentric eruptions (Magee et al., 2021). Also plotted for comparison is the starting composition for the experiments of Masotta et al., (2020), which the ΔT calibrations used in this study were calibrated. b.) Ternary diagram following the classification scheme of Morimoto (1988). Data for the Mt. Etna eruptions are from this study and experimental data is that reported in MacDonald et al., (2023)

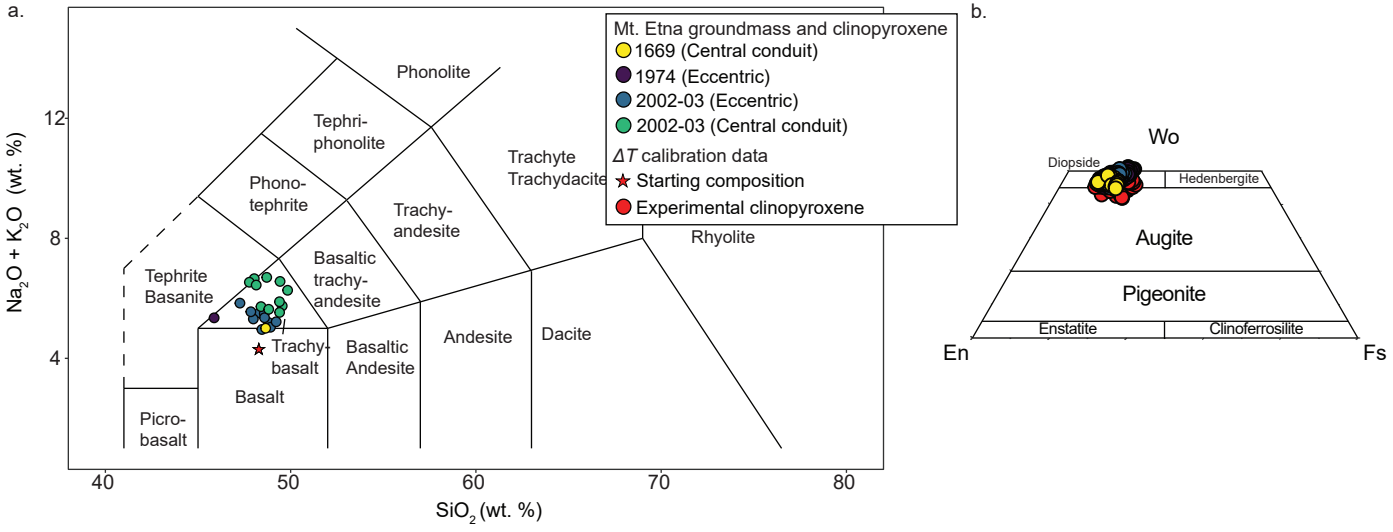

Supplementary Figure 3: Back scattered electron images of a clinopyroxene megacryst (left) and microphenocryst (right) from the 1669 flank and 1974 eccentric eruptions, respectively. Compositional contracts between hourglass and prism sectors are evident.

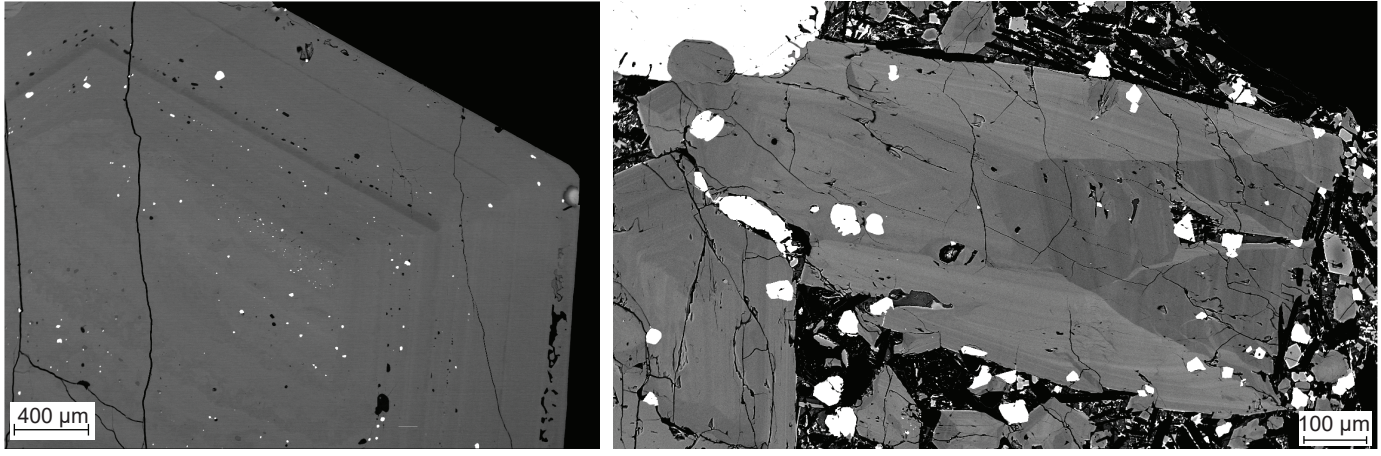

Supplementary Figure 4: LA-ICP-MS compositional maps of Cr for all clinopyroxene crystals from the 2002-03 eccentric and central conduit eruptions analysed in this study. Maps are quantitative for clinopyroxene and share an upper limit of 1000 ppm Cr to highlight the variability of Cr enrichment in mantle zones.

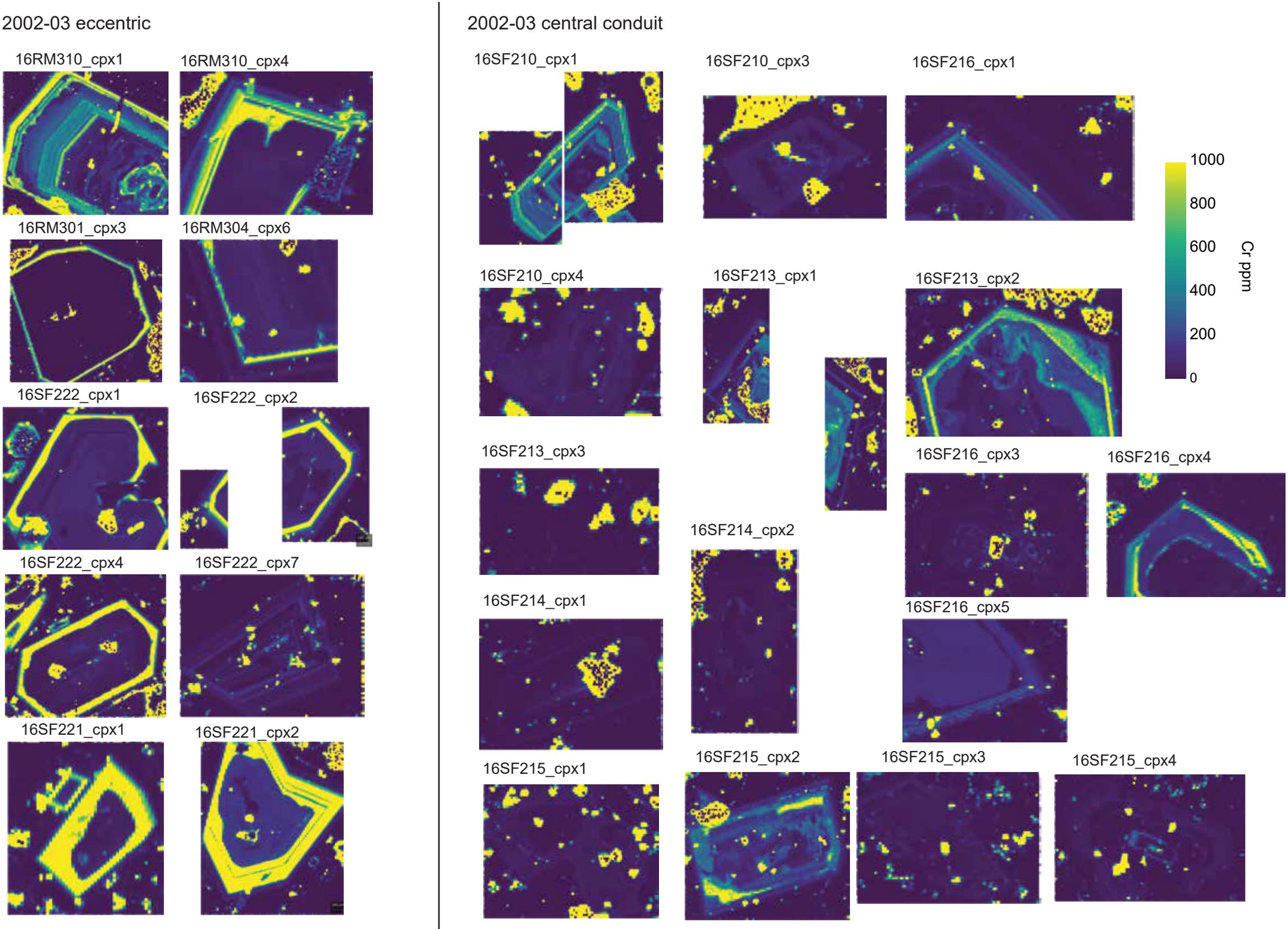

Supplementary Figure 5: Onuma curves for 3+ cations in the M2 site of hourglass sectors in clinopyroxene from the 1974 and 2002-03 eccentric and central conduit eruptions, obtained by plotting apparent partition coefficients for REE against ionic radii (Å; values from Shannon, 1976). All curves have $R^2 > 0.98$ and form near-parabolic relationships. First row: 1974 clinopyroxene micro-phenocrysts. Subsequent rows: 2002-03 eccentric (up to 16SF222_cpx7) and central conduit clinopyroxene phenocrysts.